1
Fundamental of Graphene

Seong C. Jun

1.1
Introduction

Graphene, a single-atom-thick sheet of hexagonally arrayed sp^2-bonded carbon atoms, has got a significant attention due to its unique electronic [1], mechanical [2], and thermal [3] properties all derived from the unique details of its electronic band structure. Due to its flexibility, graphene provides infinite possibilities in various fields [4, 5] and the peculiar dispersion relation of carbon's π electrons is responsible for its unique properties [1].

There are different ways to produce "pristine" graphene. The graphene synthesis can be mainly classified into exfoliation [6], chemical vapor deposition (CVD) [7], arc discharge [8], and reduction of graphene oxide (GO) [9]. One method for isolation of a sheet of graphene is through the mechanical exfoliation from a graphite crystal, but this is not scalable beyond one small flake of graphene, making graphene with lateral dimensions on the order of tens to hundreds of micrometers. But reports are also showing the development of patterned graphene through the mechanical exfoliation of patterned graphite.

The important large-scale synthesis of graphene includes the thermal decomposition of silicon carbide [10] and CVD growth. The formation of carbon layers with sp^2 bonding, on the SiC substrate could be obtained through the sublimation of Si by heating the *C*-face or Si-face in ultrahigh vacuum (UHV) at temperatures ranging from 1000 to 1500 °C and the thermal decomposition of hydrocarbons. CVD method has raised much attention for graphene synthesis due to high quality with large surface area. Gas-phase synthesis of graphene platelets and arc discharge synthesis of multilayered graphene are also reported.

Exfoliation of graphite in solvents is a method for obtaining dispersions of GO to yield individual layers of GO and offers potential for the production of cost-effective, large-scale production of graphene [9]. Based on recent studies, GO consists of phenol hydroxyl and epoxide functional groups on the top and bottom surfaces of each sheet and sp^2-hybridized carbons containing carboxyl and carbonyl groups mostly at the sheet edges and these groups offer tremendous opportunities for access to functionalized graphene-based materials [11]. The oxidation

Graphene-based Energy Devices, First Edition. Edited by A. Rashid bin Mohd Yusoff.

of graphite to GO breaks up the sp^2-hybridized structure of the stacked graphene sheets and the disruption of graphene lattice is reflected in an increase in interlayer spacing from 0.335 nm for graphite to more than 1 nm for GO. In GO, the ratio of sp^2/sp^3 fractions opens up possibilities for new functionalities and possesses a finite electronic band gap generated by the disruption of π-networks due to the formation of oxygen-containing groups. Thus, it is possible to modify the electronic structure by means of chemical or physical treatments with different gases to reduce the connectivity of the electron network [12–14]. In contrast to pristine graphene, in which all atoms are sp^2 hybridized, GO also contains sp^3 carbon atoms covalently bonded to oxygen-bearing functional groups.

Characterization of graphene involves various microscopic and spectroscopic techniques such as: X-ray diffraction (XRD), transmission electron microscopy (TEM), low energy electron diffraction (LEED), Raman spectroscopy, scanning electron microscopy (SEM), and so on. These characterization tools can be used for characterizing the structural, chemical, electrical, and even magnetic properties of graphene. The intrinsic ripples of freely suspended graphene have been addressed by Monte Carlo simulation TEM and optical microscopy studies can be used to find the number of layers and the presence of defects [15, 16]. Optical microscopy is based on the contrast arising from the interference of the reflected light beams at the interfaces. Contrast in SEM can also be used to determine the number of graphene layers [17]. Using TEM, by viewing the edges of the film, it is possible to analyze the number of layers. TEM can also be used to evaluate the number of graphene layers and to assess the crystalline quality of the graphene films [10]. TEM images provide images of sp^2 clusters as well as defects. The diffraction experiments provide knowledge of the orientation of the crystal lattice and different crystal grains can be mapped. Electron diffraction is an effective tool, in which the intensities of diffraction peaks do not change much with the incidence angle for single layer graphene. But, in bilayer graphene, there is a change in intensity with different incidence angles. Thus, by comparing the relative intensities of the electron diffraction pattern, it is possible to determine the number of layers. The thickness of graphene layers can be obtained by atomic force microscopy (AFM) in the tapping mode. Fluctuations in height for graphene platelets deposited on different Si substrate could be studied by scanning tunneling microscopy (STM).

Raman spectroscopy is the principal tool to examine the quality of graphene crystals; it is a nondestructive tool and does not require vacuum. Raman spectroscopy is a tool for finding the number of graphene layers by manipulating the position and shape of the 2D band, which is around 2700 cm^{-1}. Raman spectra of GO consists of prominent spectral features, called G at ~1586 cm^{-1}, D bands ~1350 cm^{-1}, and 2D at 2697 cm^{-1} [18]. Raman spectra of all disordered carbons are dominated by the relatively sharp G and D features of the sp^2 sites. The G and 2D peaks represent the E_{2g} vibrational and out-of-plane modes within aromatic carbon rings, respectively. The G band is a degenerated optical phonon mode at the Brillouin zone center and is induced by a single resonance process. The peak near 1350 cm^{-1} is denoted with the D band (in

plane carbon ring breathing mode (A_{1g} mode)), which is forbidden in perfect graphite. This process requires a scattering at defect sites in order to conserve the momentum. Photoluminescence (PL) in such carbon systems usually is a consequence of the recombination of localized e–h pairs in sp^2 clusters [19]. Excitation wavelength-dependent PL emission from the GO and graphene quantum dots were also observed and the PL peak shifted from 430 to 515 nm when the excitation wavelength was changed from 320 to 420 nm [13]. Bao *et al.* [20] reported intense PL from chemically modified graphene, where oxygen plasma treatment was applied to introduce band gap opening in graphene and the degree of band gap opening is proportional to the degree of oxidation. The effects of oxygen plasma treatments on the PL properties of single- and few-layer graphene (FLG) growth by the CVD process were described by Gokus *et al.*, and they observed visible luminescence from oxygen plasma-treated graphene that has been attributed the emission to carbon–oxygen-related localized states [21]. It is possible to induce ripples on the graphene surface, which can alter the local electrical and optical properties of graphene; thus, modified ripple engineering can be used for possible application in various devices.

1.2 Synthesis of Graphene

1.2.1 Mechanical Cleavage

Mechanical cleavage is one of the simplest methods to obtain graphene from highly ordered pyrolytic graphite (HOPG) ensuring its smooth edge structure. Mechanical cleavage is a general and novel method to exfoliate bulky crystals, such as hexagonal boron nitride (h-BN), or Molybdenum disulfide (MoS_2), to few-layer ultrasharp, single-crystal layer. This was the method used to exfoliate and isolate a few graphene sheets of micrometer size in the research of Andre Geim and Konstantin Novoselov of University of Manchester; they won a Nobel Prize in Physics in 2004 [6]. This method also called the *tapping method* involves the use of Scotch Tape to separate the graphene sheet from graphite flakes. Few-flakes of graphite are loaded on Scotch Tape and continuous alternation of attaching and detaching exfoliates graphite into FLG. To transfer and visualize the graphene, we need to stick the tape on a target Si/SiO_2 wafer and examine the wafer with an optical microscope. The graphene and few layers of it are almost transparent to the naked eye; however, by adding graphene layers to the Si/SiO_2 wafer, which is usually oxidized about 300 nm, the graphene interferes with the light and shifts the color; this allows us to distinguish its existence and even the layer difference from mono, or few-layer to multilayer graphene. Figure 1.1 shows how to stick graphene-exfoliated Scotch Tape to wafer, and Figure 1.1b shows the optical microscope image of a graphene-attached wafer.

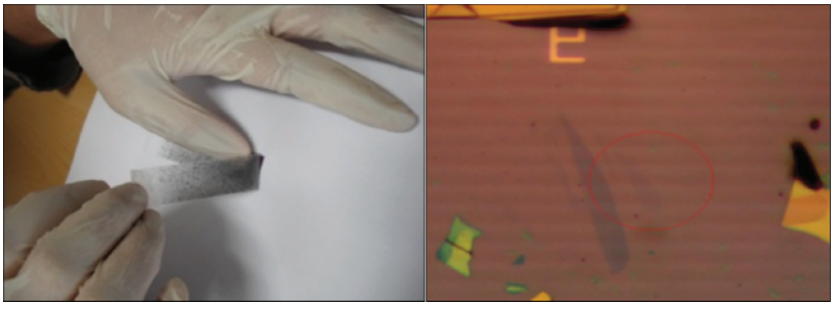

(a) (b)

Figure 1.1 (a, b) Mechanical exfoliation of graphene.

1.2.2
Epitaxial Growth

Epitaxial growth graphene has attracted tremendous attention due to the fabrication problem of mechanical exfoliated graphene. A few layers of graphite growth on SiC surface (0001) was already known by the epitaxial growth mechanism. In 1975, the graphite covering on SiC was obtained by heating the SiC crystal in oxygen at a low pressure above 1000 °C[10]. The existence of low vacuum at high temperature conditions leads to a depletion of Si, resulting in a high portion of the carbon layer turning to graphite layers. LEED patterns are usually employed to shows the states of obtained graphite layers. Annealing above typical temperatures affects reconstruction, for example, Si-rich $(\sqrt{3} \times \sqrt{3})$ R30° structure transforms into carbon-rich structure $(6\sqrt{3} \times 6\sqrt{3})$ R30° [22]. Since the reconstruction of carbon-rich structure is a precursor to graphene on SiC, that structures attract attention. The different band position of SiC and graphene or a few layers of graphene leads to barriers at the junction, affecting electrical properties including photoemission. There are around 3 eV energy gap attributed to relative position difference of band structure. Through many researches, homogeneous large area graphene are synthesized [23]. Substrates are treated chemical mechanical polishing. Then, the graphene growth process is conducted under highly isothermal conditions at very high temperatures with ambient Ar condition. Also, various substrates are employed such as Ru [24], Ir [25], and Pt [26].

1.2.3
CVD Growth of Graphene

Graphene can be grown by the CVD process on the catalytic metal substrates. Usually, metal foils, dimensions about 20 cm with thickness of few micrometres, or metal-deposited substrates are used. Various metals can be applied including Ni, Cu, Pd, which are the catalysts of carbon [7]. The metal substrate sample is then loaded in reactors of 2-in.-wide quartz tube and the temperature increased with

Ar, H_2, or its mixture condition. In case of copper, which is the most widely used, the loaded copper was heated up to 1000 °C or more, with hydrogen gas. After reaching the target temperature, the sample is then subjected to annealing; it is reported that this flattens the target surface and also affects the carbon solubility of the substrate metal. Usually, copper foil is annealed for 30 min with a sustaining flow rate and pressure of H_2 gas. Also, in the case of copper, this heat-treatment results in adequate grain size required for the making of higher-quality graphene films. After 30 min of annealing, the gas phase of carbon source including CH_4 gas or C_2H_2 gas flows with Ar/H_2 mixture, matching the unique recipe that depends on the metals or gas mixture rates. By this step, carbon from the gas source is diffused into the copper foil. The process is terminated by enabling far rapid cooling to room temperature, usually without the flowing of the carbon source gases. After the rapid cooling process, the diffused carbon from copper comes on the surface and a monolayer of carbon hexagonal film formed as graphene.

The graphene film that is grown on metal films or substrates is then transferred on to the target substrate [27]. The most general and widely used technique is to use the PMMA (polymethylmethacrylate) polymer. The PMMA is coated on graphene-metal substrates and then the metal is etched out using a specific etchant. The isotropic wet etching removes metal and some graphene residue from the bottom surface of the metal substrates. The remaining PMMA-graphene film on the metal etchant is then rinsed with deionized (DI) for 1 or 2 days, thereby ensuring that there is no Cu etchant residue on its surface and transferred carefully on to the target substrate. The substrate then goes through cleaning and annealing with high vacuum and temperature conditions for removing PMMA adhesion. Generally, to confirm the purity of the graphene film on a target substrate, Raman spectroscopy and other versatile characterizations (electrical resistance or optical transmittance in a visible region) are used.

The Figure 1.2 shows schematic of graphene growth process. In case of the picture on the right, the graphene sample was grown on Cu foils, 50 μm thick at temperatures of 1000 °C with carbon obtained from a mixture of methane (CH_4) and hydrogen (H_2) gas and transferred on Si/SiO_2 with PMMA and Cu etchant. The SEM image shows the uniform deposition of graphene on the substrate and the bottom picture shows that graphene is transferred to the Si/SiO_2 substrate.

1.2.4
Solution-Based Graphene

In the nineteenth century, graphite oxide was synthesized by the Brodie, Staudenmaier, and Hummers methods [9]. From then on there have been various preparation methods of solution-based graphene including not only chemical methods but also a physical method. Exfoliating graphene with solution processes was in practice since the material attracted tremendous attention because of its advantages. Moreover, solution-based graphene has many advantages of fabricating devices such as roll-to-roll and printable processes especially with regard to mass production. Solution-based graphene synthesized by the above-mentioned

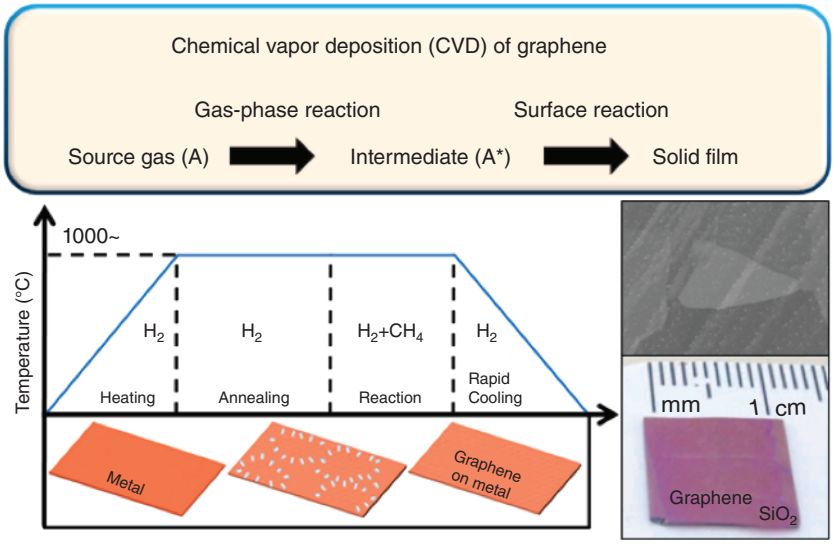

Figure 1.2 Chemical vapor deposition process of graphene.

methods are exfoliated from graphite, which is one of the allotropes of carbon, piled up on graphene layers with AB stacking. The idea of exfoliating graphene from graphite originated due to the weakening interaction between the layers.

1.2.4.1 Ultrasonication

Graphene dispersion prepared by the physical method is exfoliated by horn ultrasonication of natural graphite flakes in an aqueous solution with sodium cholate as a stabilizing agent and density gradient ultracentrifugation [28]. Compared with the covalent bonding of carbons in a graphene monolayer sheet composed of benzene rings, each graphene flake is combined by van der Waals force due to the interaction of p_z orbitals of carbon atoms in graphene; these combinations are possibly broken by horn ultrasonication. However, since these separated flakes are hydrophobic they gather as colloid; sodium cholate is dissolved in the solution to disperse graphene flakes. The hydrophobic face of sodium cholate is combined with the graphene flakes, while the hydrophilic face is combined with an aqueous solution consisting of liposome followed by sedimentation centrifugation to remove the thicker flakes that are broken imperfectly by horn ultrasonication. Then, by density gradient ultracentrifugation, it is possible to separate the exfoliated graphene with different thicknesses. The average thickness of the graphene flakes with the least buoyant density is around 1 nm measured by AFM. Also, graphene flakes having different layers are confirmed by Raman shift by comparing the intensity of G band and 2D band. The graphene flakes obtained from physical methods have D band-related disorders, which are due to the defect present within the flakes and because of their tiny size.

1.2.4.2 Intercalation

Another physical method for exfoliating graphite is the potassium-intercalation process [29]. Naturally occurring graphite is accumulated in AB stacking and carbon atoms of the upper graphene layer are positioned within the center of the benzene ring of the lower graphene layer. Alkali metals easily intercalate the layered structure of graphite, affecting the interlayer spacing related to the van der Waals force. However, graphene flakes exfoliated by intercalation shows low yield and are unstable.

1.2.4.3 Chemical Exfoliation

On the other hand, the chemical method needs oxidants, such as oxygen atoms, to break the interaction between the graphene flakes. As mentioned earlier, graphene flakes are combined by van der Waals force, that results from the π interaction of the different layers of graphene flakes. When carbon atoms composed benzene rings repeated, the orbitals of carbon hybridize each other, changing sp^3 orbitals to sp^2 and p_z orbitals. Comparing sp^3 shows three-dimensional structures; sp^2 exhibits planar shapes and combines each carbon as a σ bond. The remaining orbital, p_z of each carbon, composes delocalized electron clouds, which affect the van der Waals force. Therefore, if the delocalized orbitals are affected by the different bonding combinations, the force between the flakes becomes weak. Usually, by using oxidants, oxygen atoms are effective on the forces. In the chemical exfoliation method, strong acids and oxidants are used to synthesize GO. In recent days, the Hummers method is the most employed with some modifications made. Naturally occurring graphite powder is used to synthesize graphite oxide, which is the primary stage of material (GO), having weaker bonding than normal graphite states. The modified Hummers method comprises two-step oxidation processes. After the pre-oxidation step using potassium peroxodisulfate and phosphorus pentoxide in sulfur acid condition, pre-oxidized graphite that is aged a few hours is oxidized again with potassium permanganate, followed by filtering and washing with HCl for eliminating metal ions from oxidants. Next, the oxidized graphite in membrane filter is dialyzed by stirring distilled water to purify the residual salts and acid. The suspension is sonicated for exfoliation and centrifuged for removing the graphite powder that is not reacting with the oxidant. However, GO suspension, well dispersed in purified water, shows relatively lower properties than graphene due to the lower number of participating delocalized carriers resulting from oxygen-related functional groups including carboxyl, carbonyl, and epoxide groups. According to previous researches, these functional groups are placed in different positions such as phenol hydroxyl and epoxide groups on both the surfaces, and carboxyl and carbonyl groups at the edges of flakes [11]. These groups makes GO with tuneable properties for various application. In order to reduce GO, thermal and chemical reduction means are employed [30, 31]. rGO, which retains the properties of single-layer graphene can be fabricated on a device with reduction at various conditions, regulated by vaporized hydrazine or high temperature annealing under noble gas condition.

Suspension state GO is normally reduced by chemical modification by mixing various chemicals such as hydrazine, hydroquinone, and $NaBH_4$. These reduction methods change the atomic ratio of GO from sp^3 bond composed of carbon and oxygen to sp^2 bond of benzene rings demonstrated with elemental analysis, Raman spectroscopy, and X-ray photoelectron spectroscopy (XPS). The changes reveal various properties, since carboxyl and hydroxyl groups decreases with the reduction process. The deconvolution of XPS shows a different ratio since the bonding ratio between carbon to carbon bond and carbon to oxygen changes. Also, the vibration-scattering changes according to orbital transition effects on Raman scattering peak the intensity ratio. GO naturally exhibits negative charges that come from ionized functional groups, which make it disperse in water easily. Hexylamine-modified graphene is obtained using an amine within the methanol solution before the hydrazine reduction process [32]. Modified graphene contains more nitrogen atoms than unmodified graphene measured by element analysis and XPS, thereby showing more intensity of carbon and nitrogen. Since amine groups on graphene flakes reveal positive charges when the ligand is ionized, different applications can be adapted. Also, layer-by-layer graphene tends to show strong interactions rather than the same charged functionalized graphene.

1.2.5 Synthesis of Composite Material Based on Graphene Oxide

Nano composites or hybrid materials have inspired passionate research over past decades because of their new optical, electronic, thermal, mechanical, and catalytic properties. Graphene-based materials can be prepared for composite with various other materials, such as metal, polymer, and biomolecule. Forming composite with pristine graphene sheet has known to be difficult, because it is chemically stable and nonactive. In contrast, GO has many functional groups including oxygen, which is helpful for bonding with other particles; hence, it is more used for synthesis of composite. Hybrid materials of graphene sheet have been studied for its modified energy level distribution, which causes to improve its characteristics. Numerous research groups have tried to prepare graphene and metal or metal oxides decorated graphene. This has resulted in a novel kind of composite material and possibly brought in new functionality and properties [33–36].

The demonstration of structural property and chemical bonding between graphene sheets and inserted material can be facilitated by various measurements, such as XPS, XRD, TEM, SEM, and so on. The TEM and SEM are high-resolution imaging techniques for monitoring the surface profile of materials. XRD is helpful to confirm the structure of materials. And XPS measures the bonding energy between atoms for observing the chemical relation. Furthermore, many detecting methods exist such as electron energy-loss spectroscopy (EELS), high resolution transmission electron microscope (HR-TEM), high-angle annular dark-field (HAADF)-scanning transmission electron microscope (STEM), and energy dispersive spectroscopy (EDS). According to the material state, we should choose the proper experiment [13, 37–39].

The studied metals are gold, silver, copper, cobalt, nickel, palladium, titanium, and so on. There is no end to this list. Also the states of metals are various, for example, homogeneous nanoparticle (NP), ion, and molecule composed of metal cation and anion. Particularly, Ag is considerably exploited for synthesis with graphene/GO [40]. Thus, many preparation methods are reported and widely used for advanced experiments. Ag/graphene composite exhibits the catalytic activity for the oxygen-reduction reaction of graphene and can become a cathode in alkaline fuel cells because it can help to solve the methanol cross-over problem from the anode. Also, optical property of Ag/graphene can be modified by the interaction between orbitals in Ag and carbon atoms [40, 41].

The preparation of graphene with metal nanoparticles hybrid material usually, done by using chemically mixing and heating or vapor deposit. Thus, an extremely important factor is the condition under which the experiment is done – conditions such as temperature, concentration of solution, operating time – because these conditions contribute to the exfoliation of graphene sheets and NP dispersion. The methods of synthesis for Ag/graphene developed earlier are going to be discussed in this chapter. The method for Ag/graphene involves use of reduced GO, which closer to graphene, for facile synthesis. The GO was adsorbed on the 3-aminopropyltriethoxysilane-modified Si/SiO_x substrate. Then, the GO reduced to form rGO. The Ag particles are grown on the reduced GO by heating them at 75 °C for 30 min in $AgNO_3$ solution. The reduced GO becomes decorated with Ag particles. Another method is that $Ag[(imH)_2]NO_3$ was added in the NH_3 solution with dispersed GO at a pH of 9.5. The compound of Ag complex and GO was heated in the nitrogen atmosphere as inert gas. The TEM image in Figure 1.3 shows an Ag NP grown on the single-layer GO surface.

Similarly, samples having Au can be produced by adding $[Au(bipy)Cl_2]NO_3$ with heating raised temperature until 573 K at a rate of 5 K min^{-1}. Other transition metals can build a composite with GO, such as Co, Ni, and Cu with Ammine complexes $[Co(NH_3)_6]^{3+}$, $[Ni(NH_3)_6]^{2+}$, $[Cu(NH_3)_4]^{+}$, which were used as intercalates to create the precursors and metal-decorated graphene. Figure 1.4 represents the TEM images of Cu–Gr heated at 673 K (Figure 1.4a), Co–Gr heated at 673 K (Figure 1.4b), and Ni–Gr heated at 673 K (Figure 1.4c). These images resemble the images of Pt, Pd, or Ru samples that we reported. Micropore or mesopore was not discovered on the carbon surface. Therefore, the mesoporous structure estimated by the isotherm measurement is responsible for the room between exfoliated graphene sheets and the empty space in wrinkled parts on the graphene sheets. Redox reaction between GO and Fe^{2+} is preparation route for Fe_3O_4/rGO composite (reduced graphene oxide). Redox reaction of GO with Fe^{2+}, in water/NH_4OH (pH 9) solution and collected by applying magnet.

Composites combine not only with metal but also with a kind of polymer. Functional groups, for instance, alcohol, aldehyde, ester, carboxylic acid, and amide, on the GO surface are beneficial for chemical reaction. The polymer as multiphase solid material has also various functional groups and these can assist bonding

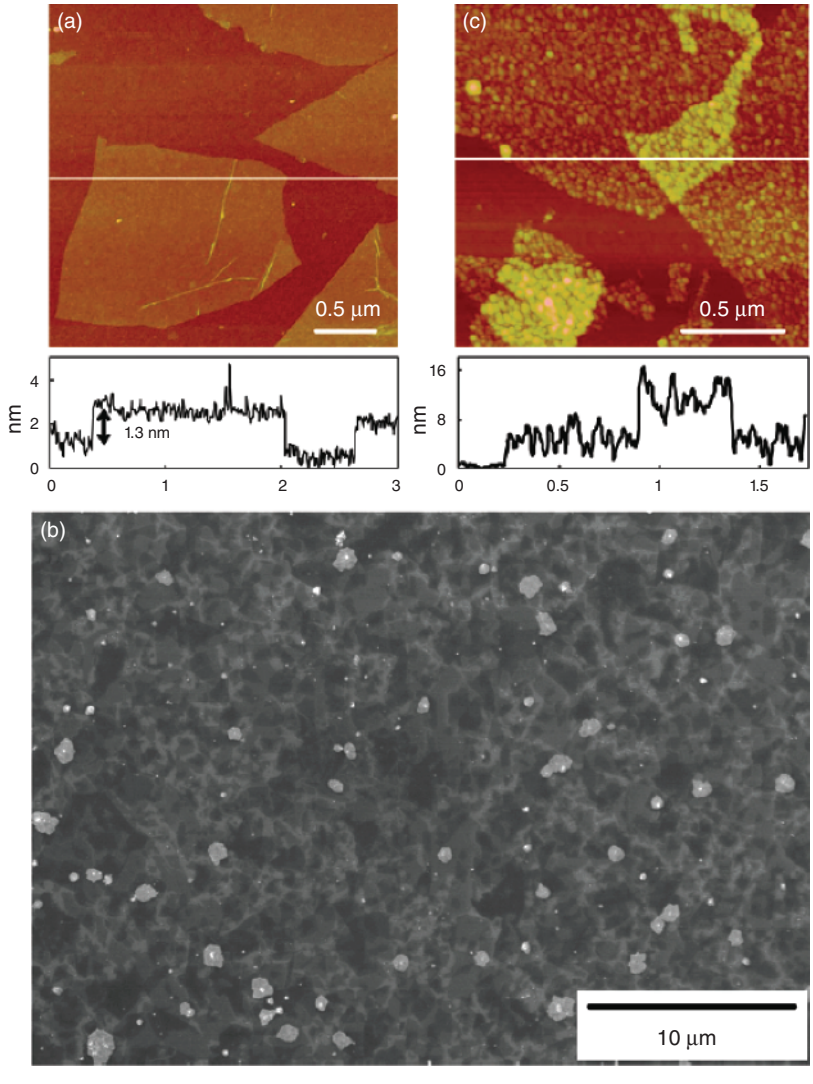

Figure 1.3 (a) Tapping mode AFM topographic image and height profile of single-layer GO adsorbed on APTES-modified SiO_x substrate. (b) SEM image of Ag particles grown on rGO surface. (c) Tapping mode AFM topographic image and height profile of Ag NPs grown on single-layer GO surface.

with other materials [39, 42]. Many research programs in this field used polymer for sensing, bonding, and filtering by the characteristic of selective attachment. They developed numerous devices to interact with biomolecules like protein, DNA, and metal particles. The graphene and polymer composite provides a way to the production of a wide innovative class of graphene-based materials and their use in a variety of applications. This chapter presents the general method

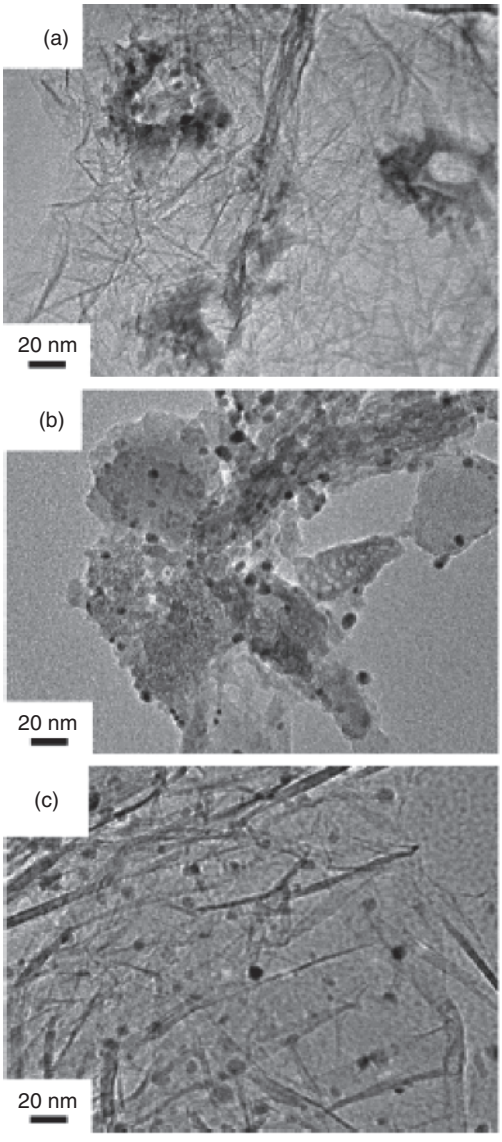

Figure 1.4 TEM images of Cu–Gr heated at 673 K (a), Co–Gr heated at 673 K (b), and Ni–Gr heated at 673 K (c).

of graphene–polymer composites by exfoliation of graphite and dispersion in polymer at molecular scale. For example, a polystyrene–graphene composite, the electrically conductive graphene–polymer nanocomposites, is formed by the solution phased mixing of the exfoliated phenyl isocyanate-treated graphite oxide sheets with polystyrene, followed by their chemical reduction. These composites represent the individual graphene sheets well dispersed via the polymer matrix.

Similar performances have been accomplished with other styrenic polymers such as acrylonitrile-butadiene-styrene and styrene-butadiene rubbers. Chemical reduction was indispensable for inducing electrical conductivity because composite samples become insulating before phenyl isocyanate–treated graphite oxide sheets were reduced. In addition, the existence of the polymer in solution during the reduction process contributes to preventing the agglomeration among the sheets because the sheets of GO covered with the polymer. The graphene–polymer composite fabrication process starts from preparation of graphite oxide sheets by exfoliation graphite powder. After graphite oxide sheets are treated with phenyl isocyanate, they are mixed with dissolved polystyrene in dimethylformamide (DMF). Composite powder obtained from coagulation of graphene and polymer through reduction by *N*,*N*-dimethylhydrazine in methanol. In Figure 1.5, the morphology of graphene/polysterene composite is represented by SEM and TEM images. In addition, many other modifying methods with polymers report that characteristics are improved based on the agent used. Some methods are introduced that graphene makes composite with octadecyl amine by reduction in the stabilization medium and with poly-L-lysine by covalent modification with alkyl amine/amino acid by nucleophilic substitution. We can benefit from the advantages of these methods such as enhancing conductivity as well as capacitance, mechanical property, and heat capacity.

Lastly, some other atoms such as europium in lanthanoids and palladium are used for composite with graphene-based material [39]. These composites demonstrated the PL characteristics in visible light range and opened the possibility of display device material. Similarly, these atoms combined due to chemically mixing in solution and annealing. The performance of PL with heat and oxygen plasma treated GO is explained in a later chapter.

1.3 Characterization of Graphene

Graphene, a single-atom-thick sheet of hexagonally arrayed sp^2 bonded carbon atoms, has been able to get significant attention due to its unique electronic, mechanical, and thermal properties all derived from the unique details of its electronic band structure. On the basis of recent studies, GO consists of phenol hydroxyl and epoxide functional groups on the top and bottom surfaces of each sheet and sp^2 hybridized carbons containing carboxyl and carbonyl groups mostly at the sheet edges and these groups offer tremendous opportunities to access functionalized graphene-based materials. The oxidation of graphite to GO breaks up the sp^2 hybridized structure of the stacked graphene sheets and the disruption of graphene lattice is reflected in an increase in interlayer spacing from 0.335 nm for graphite to more than 1 nm for GO. In GO, the ratio of the sp^2/sp^3 fractions opens up possibilities for new functionalities and possesses a finite electronic band gap generated by the disruption of π-networks due to

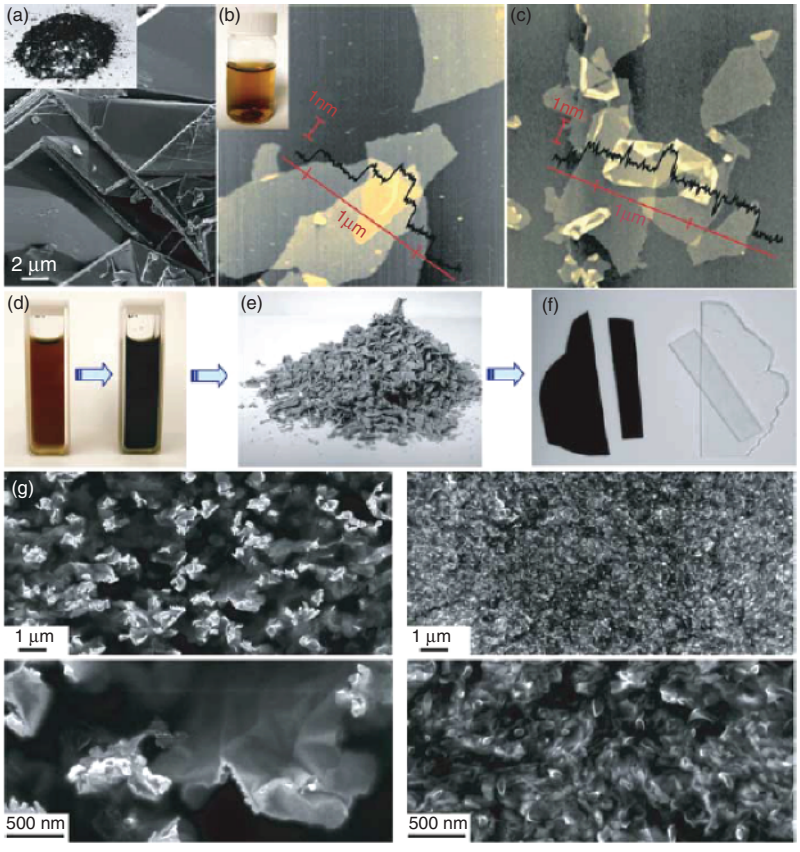

Figure 1.5 Process flow of graphene–polymer composite fabrication. (a) SEM and digital image (inset) of natural graphite. (b) A typical AFM noncontact-mode image of graphite oxide sheets deposited onto a mica substrate from an aqueous dispersion (inset) with superimposed cross section measurements taken along the red line indicating a sheet thickness of, 1 nm. (c) AFM image of phenyl isocyanate-treated graphite oxide sheets on mica and profile plot showing the, 1 nm thickness. (d) Suspension of phenyl isocyanate-treated graphite oxide 1 mg ml^{-1} and dissolved polystyrene in DMF before (left) and after (right) reduction by *N*,*N*-dimethylhydrazine. (e) Composite powder as obtained after coagulation in methanol. (f) Hot-pressed composite (0.12 vol% of graphene) and pure polystyrene of the same 0.4-mm thickness and processed in the same way. (g) Low (top row) and high (bottom row) magnification SEM images obtained from a fracture surface of composite samples of 0.48 vol% (left) and 2.4 vol% (right).

the formation of oxygen-containing groups. Thus, it is possible to modify the electronic structure by means of chemical or physical treatments with different gases to reduce the connectivity of the electron network. TEM can also use to evaluate the number of graphene layers and to assess the crystalline quality of the graphene films. TEM images provide images of sp^2 clusters as well as

defects. The diffraction experiments provide knowledge of the orientation of the crystal lattice and different crystal grains can be mapped. Raman spectroscopy provides information about the number of graphene layers and can provide information about the differences between HOPG, FLG, and graphene. PL spectra can be used to understand the sp^2 and sp^3 clusters. In contrast to pristine graphene, in which all atoms are sp^2 hybridized, GO also contains sp^3 carbon atoms covalently bonded to oxygen-bearing functional groups and the PL in such carbon systems usually is a consequence of recombination of localized e–h pairs in sp^2 clusters. Excitation wavelength-dependent PL emission from the GO and graphene quantum dots were also observed and the PL peak shifted from 430 to 515 nm when the excitation wavelength was changed from 320 to 420 nm.

1.3.1 AFM (Atomic Force Microscopy)

This measurement method of imaging can effectively represent the surface profile at the nanometer scale. AFM is a scanning probe microscopy type with very high resolution, in the order of fractions of a nanometer, more than 1000 times better than the optical diffraction limit. However, this method is not suitable for imaging large regions of material. The profile is obtained by interaction between the surfaces with a mechanical probe. Piezoelectric elements are used for accurate and precise movements and sensing the force by electronic signal change [43, 44]. Imaging modes are mainly of two types – the static mode with the deflection of the cantilever and the dynamic mode that uses the vibration at the fundamental resonance frequency. In the static mode operation, the tip is connected to the surface of the sample as close as needed. Thus, static mode AFM, which is always conducted in contact with the entire force, is repulsive. The force is maintained constant during dragging on the surface to notify deflection.

In the dynamic mode, the tip of the cantilever stays a distance from the sample surface. The cantilever oscillated at its resonance frequency, where the amplitude of oscillation is typically between few picometer to few nanometer (<10 nm) [45]. Above the surface, the van der Waals forces or any other long-range force performances act to decrease the resonance frequency of the cantilever. From this derivation, measuring the tip-to-sample distance at each point of scanning area leads to building the topographic image of the sample surface. This method, called *noncontact AFM*, is a preferred method to contact AFM for measuring soft samples, for example, biology sample and organic thin film, because noncontact mode AFM does not cause damage to the tip or sample degradation effects that are sometimes observed after taking overflowing scans with contact AFM.

Distinguishing between the GO and the graphene layers in the AFM image is difficult just using the topographic contrast factor. Phase imaging, which is tapping-mode AFM, allows the separation of both the materials [46]. The separation is possible, because the AFM tip undergoes a different force with

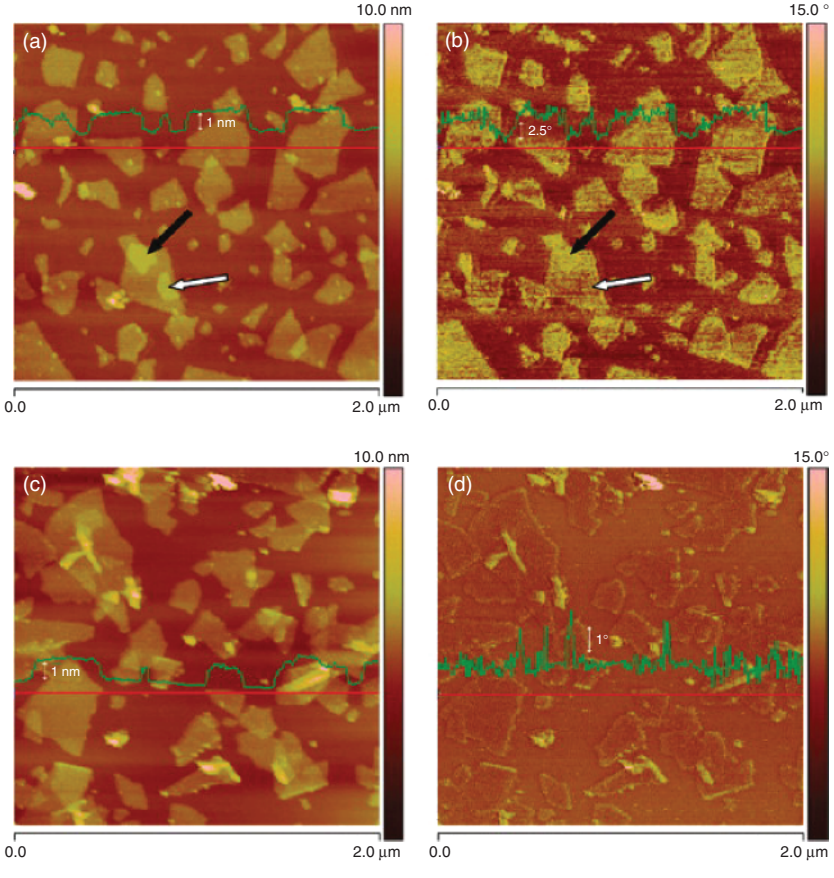

Figure 1.6 Height (a, c) and corresponding phase (b, d) tapping-mode AFM images of unreduced (a, b) and chemically reduced (c, d) graphene oxide nanosheets deposited from aqueous dispersions onto freshly cleaved HOPG. The images were recorded in the attractive regime of tip sample interaction. Superimposed onto each image is a line profile taken along the marked red line.

pristine graphene and its functionalized group. The thickness of two-dimensional materials, particularly graphene, can be measured by AFM using the repulsive mode [47]. The thickness of the unreduced GO is ~1.0 nm and that of chemically rGO is 0.6 nm. This difference in the thickness and the phase contrast arises from the hydrophilicity difference due to the distinct oxygen functional group in the reduction process as represented in Figure 1.6 [19, 48].

In the previous research, AFM has been exploited for mechanical and structural characterization of graphene because it can feel the small force from the tip of the probe [48]. In the future, new AFM modes will be developed and other modes for graphene are already suggested about mechanical, frictional, electrical, magnetic, and even elastic properties of graphene flakes (Figure 1.7).

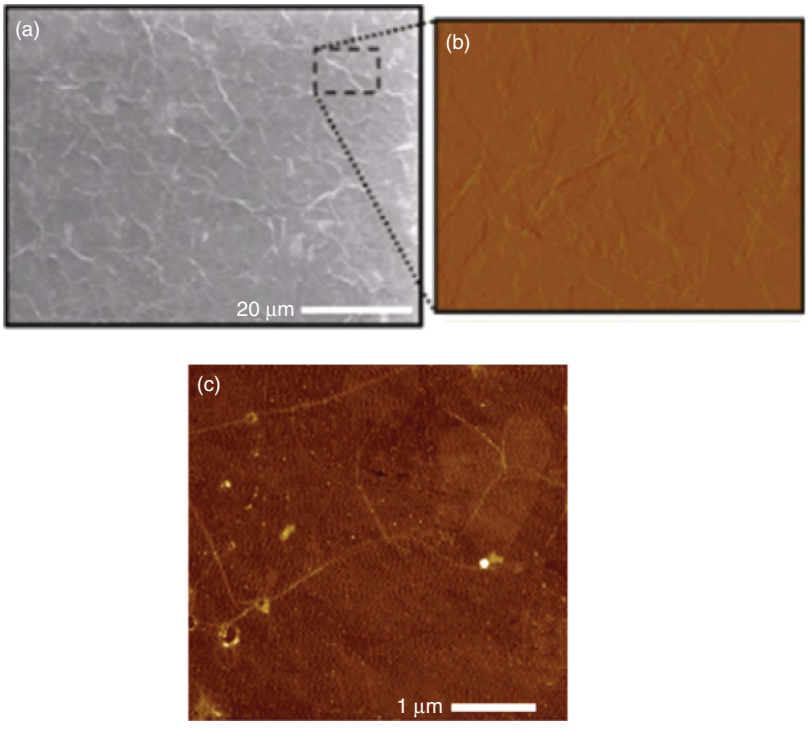

Figure 1.7 (a–c) AFM images of GO film and graphene transferred onto a fused silica substrate.

1.3.2 SEM

Graphene or GO deposited on substrates need to be morphologically characterize for more analysis. SEM is employed in order to obtain more detailed information. The number of not only graphene but also functionalized graphene layers can be classified by using this method under highly optimized conditions [17, 49]. Since, distinguishable contrast between graphene and non-graphene position reveals defects, edges and wrinkles on the surface. Graphene is easily detected because it has high mobility, and it shows as a semimetal. However, the SEM image shows representative electronic structures rather than topology because of its semimetallic property.

1.3.3 TEM/SEAD/EELS

GO sample was deposited on the standard holey-carbon-film-covered copper grids and loaded into the microscope for TEM measurements to study GO lattice. HR-TEM images of pristine GO and oxygen plasma–treated GO with different

oxygen pressure illustrate that, atomic structures get in order at an optimum oxygen pressure and disordered thereafter (Figure 1.8a and 1.24b). TEM images show that during the oxygen plasma treatment, the thermal energy favors the further clustering of the sp^2 phase, thereby stimulating the connection between ordered rings and oxygen atoms attached to graphene sites randomly and convert sp^2 carbon bonds to sp^3 bonds. Thus, initially the sp^2 clusters in GO are small and separated by an amorphous and highly disordered sp^3-bonded matrix, which forms a high tunnel barrier between the clusters. During heat treatment, the thermal energy favors the further clustering of the sp^2 phase, thereby stimulating the connection between ordered rings and moving from polycrystalline to the two-dimensional nano-crystalline graphene.

From the selective area electron diffraction (SAED) pattern, a typical sharp, polycrystalline ring pattern is obtained for GO-1 film (inset of Figure 1.8a). Strikingly, clear diffraction spots are observed (GO-3) characteristics of internal short-range crystalline order; the sixfold pattern is consistent with a hexagonal lattice (inset of Figure 1.8b). This simple hexagonal pattern of sharp spots is similar to that obtained from graphite oxide and leads immediately to several conclusions that the GO films are not completely amorphous and the lack of any diffraction spots other than those corresponding to the graphite structure shows that any oxygen-containing functional groups present do not form super lattice-type ordered arrays. This implies that an appreciable fraction of oxygen atoms is involved in linkage between carbon atoms. However, for GO-4 (inset of Figure 1.8c) the pattern again shows disordered nano-crystalline pattern when compared to GO-3. Also the existence of some disorder is obvious from the broadening of the diffraction spots. This broadening shows that a disturbance exists in the stacking of the closely packed planes. A similar behavior is also observed for the electron diffraction patterns of graphite.

First diffraction rings in GO have a lattice spacing of 0.76 nm, which have been identified to be the (110) reflections. After oxygen plasma treatment, the corresponding spacing are 2.1 and 2.4 nm respectively, which is larger than the interplanar spacing of pristine GO. This can be attributed to the presence of oxygen functional groups on the GO layers. The EELS spectrum, as shown in Figure 1.9, the carbon K-edge region shows a peak at 285 eV that corresponds to transitions from the 1s to the π^* states ($1s-\pi^*$), and a peak at 291 eV that corresponds to transitions from the 1s to the σ^* states ($1s-\sigma^*$). Figure 1.9a shows $1s-\pi^*$ transitions as oxygen plasma treated (GO-3, GO-4). The higher-order π^* and σ^* resonances in GO at ~292.5 and ~293.5 eV may be assigned mainly to the presence of carbon atoms bonded to oxygen atoms by epoxide and carbonyl bonds. Lower energy plasmon excitations are observed from the films in Figure 1.9b. Previous reports show that for monolayer GO, the plasmon energy of the pristine GO sheet is at 24.5 eV and the plasmon energy decreases almost linearly with sp^3 fraction. sp^3 hybridization induced by oxygen-containing groups increases this value in GO. The experimentally recorded $\pi^* + \sigma^*$ plasmon energies for a single-layer and five-layer graphene are 16.6 and 18 eV respectively. Thus, in the present study, a plasmon energy of 19.2 eV corresponds to four to six layers of GO. Thus, GO-3 and

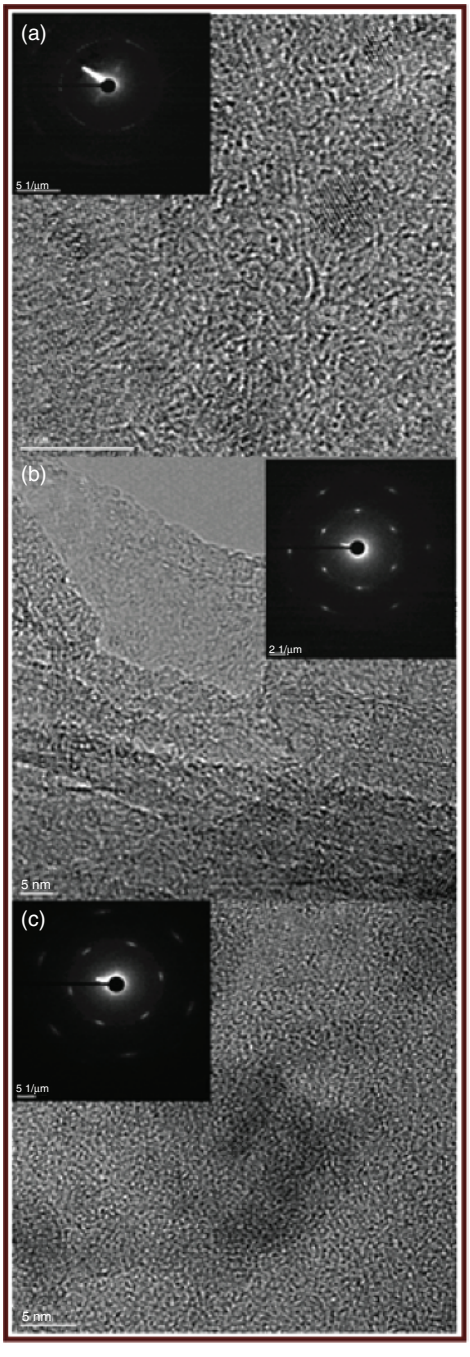

Figure 1.8 HR-TEM images of (a) GO-1, (b) GO-3, and (c) GO-4 films. Inset shows the corresponding SAED pattern.

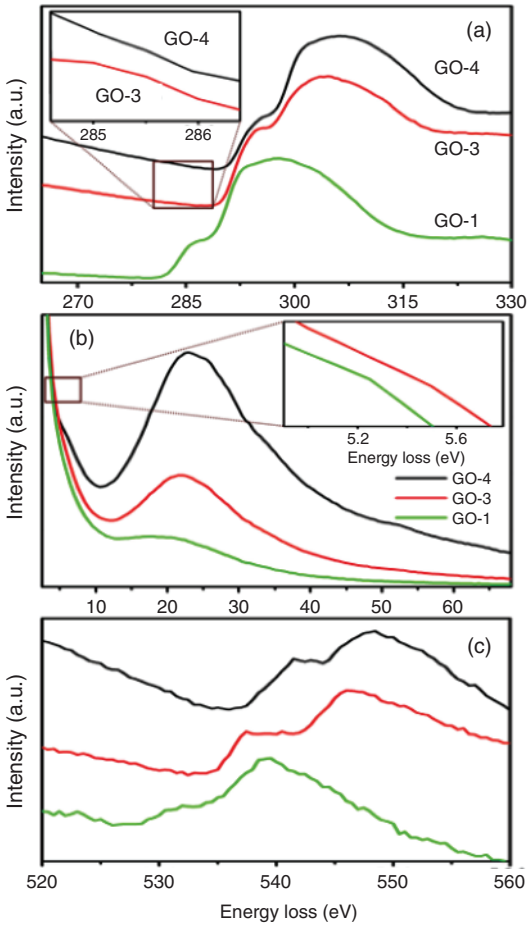

Figure 1.9 (a) EELS analysis of C K-edge, (b) lower energy plasmons resonance of GO-1, GO-3, and GO-4 films, and (c) shows O K-edge spectrum of GO films. Inset of (a) shows 1s–π* transitions from GO-3 and GO-4 films. Inset of (b) shows low energy plasma excitations of π* electrons in the GO-1 and GO-3 films.

GO-4 samples in Figure 1.9b give peak values of around 21 and 22 eV respectively and reports show that the plasmon energy of an amorphous carbon of ~45% fraction of sp^3 bond is around 24 eV. This confirms that the oxygen plasma treatment increases sp^3 bonding. The low-energy plasma excitations of π* electrons in the GO film is ~5.2 eV (Figure 1.9b) and the π* electrons in single-layer GO is ~5 eV, which shows that our film consists of three to five layers of GO. GO-1 shows a peak around 539.7 eV in Figure 1.9b,c; this may possibly be due to higher-order π* resonance of all oxygen atoms and higher-order σ* resonance of the 1,2-epoxy linkages in the GO sample. In the GO-3 film, the absorption corresponds to a peak value of ~536.7 eV and this seems to arise from σ* and higher-order π* resonances

of only epoxy bond. Peak corresponds to 545 eV and this arises from the oxygen atom from the C═O and O–C═O groups; the intensity of this peak increases, which shows the dominance of carbonyl groups in the advanced oxidation stages.

1.3.4 XPS

The XPS analysis shows us the bonding distribution through the intensities of each binding energy. In the case of graphene, the C–C bonding of sp^2 carbon in 284.8 eV is shifted from the oxidized defect in GO. In Figure 1.10a, the XPS results reveals two different peaks of carbon bonds (sp^2) and its intensity decreases with plasma-oxidation treatment for CVD graphene. In most cases, the CVD graphene has its own inherent defect from its fabrication process, which makes it difficult to have the single Gaussian peak only for sp^2 carbon. Figure 1.10b shows the XPS results of GO, which correspond to sp^2 carbon at 284.8 eV, and the other C═O or O–C═O around 288 eV. Especially, dramatic depressed sp^2 carbon peak rather than CVD graphene shows the formation of oxygen-related defects. Generally, there are several different functional groups in GO, which are characterized by the appearance of several XPS spectral peaks. The XPS C1s spectra of GO consist of four peaks that correspond to sp^2 carbon at 284.8 eV, O–H/O–C–O at 286.2 eV, C═O at 287.8 eV, O–C═O at 288.5 eV and COOH groups at 289.3 eV. The peak at 290.2 eV is from plasmon, which is a collective behavior of delocalized valence electrons of GO. It can be considered that the main bonding configuration of carbon atoms in the film is C–C. A sheet of GO consists of a hexagonal ring–based carbon network having both sp^2 hybridized carbon atoms and sp^3 hybridized carbons bearing hydroxyl and epoxide functional groups on either side of the sheet. Thus, the sp^2 clusters in GO vary in size and separated by an amorphous and highly disordered sp^3 bonded matrix, which forms a high tunnel barrier between the clusters.

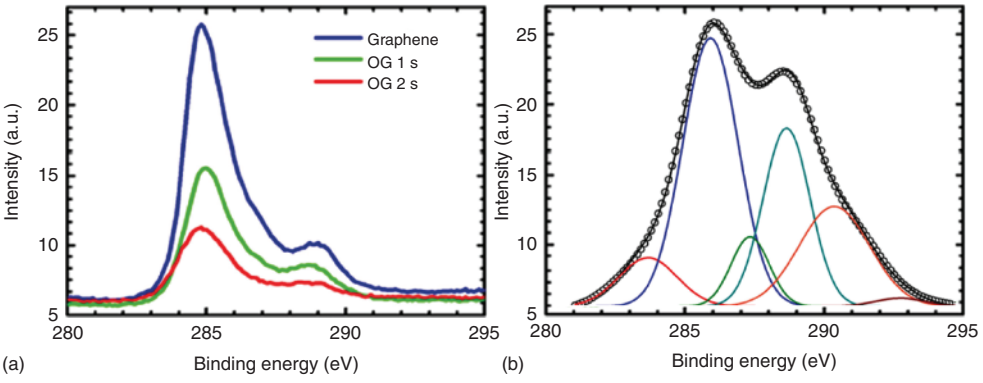

Figure 1.10 (a, b) XPS of graphene and graphene oxide.

1.3.5 XRD

XRD is used for confirming the material structure of a crystal by measuring the angles and intensities of these diffracted beams [50–52], in which the crystalline atoms lead a beam of X-rays to diffract into many specific directions. This measurement can expect the spatial density of electrons in crystal because X-ray beam interact with electrons. From this expectation, the mean positions of the atoms in the crystal can be estimated; also their chemical bonds, their defect and various other information [53–55] can be deduced. There are many crystalline materials, for example, salts, minerals, metals, semiconductors as well as inorganic, organic, and biological molecules. XRD measurement plays a key role for characterization of these materials, such as the size of atoms, the lengths and types of chemical bonds, and the atomic-scale differences among the combined materials [56–60].

For measurement, a crystal lies on a goniometer and gradually rotated while being emitted with X-rays, gathering a diffraction pattern of regularly spaced spots known as *reflections*. X-ray crystallography is related to several other methods for determining atomic structures. Similar diffraction patterns can be obtained by scattering electrons or neutrons, which are likewise interpreted as a Fourier transform.

XRD gives three types of structural information of graphene materials – the interplane distance of the lattices, graphene material thickness and the number of graphene layers. First, the base principle of XRD for material is Bragg's law [61], $n\lambda = 2d_{(hkl)}\sin\theta$, where λ is the wavelength of the X-ray, θ is the scattering angle, n is an integer representing the order of the diffraction peak, d is the interplane distance of the lattices, and (hkl) are Miller indices. Graphite or multilayered graphene has (002) planes; d_{002} becomes the interlayer distance. Scattering from entering X-ray occurs on each graphene plane. As changing the incoming angle, the X-ray beam undergoes path length difference by multiplying n (integer) of the beam wavelength λ. The beams scattered among the adjacent graphene planes could combine practically. Consequently, the XRD peak of the (002) facet of graphene exhibit a d_{002} value and the clue acquired for the lattice size and quality.

Using Sherrer's equation [61], the graphene thickness can be expected, which is expressed by $D_{002} = K\lambda/B\cos\theta$, where D_{002} is the thickness of crystallite, graphene thickness, K is a constant dependent on the crystallite shape (0.89), λ is the X-ray wavelength, and B is the full width at half maximum (FWHM), and θ is the scattering angle [61]. From Sherrer's equation, the number of graphene (N_{GP}) layers can be determined using the following equation (Ju *et al.*, 62): $N_{GP} = D_{002}/d_{002}$. From XRD crystallography, we can understand the formation during the GO reduction and the finally reduced graphene. The interlayer distance of graphene-based materials is different because there are many defects, nanoholes, and intercalated molecules, which are oxygen-bonded functional groups and H_2O molecules. The materials composed with smallest interlayer distance is graphite, 3.348–3.360 Å [63], as shown in

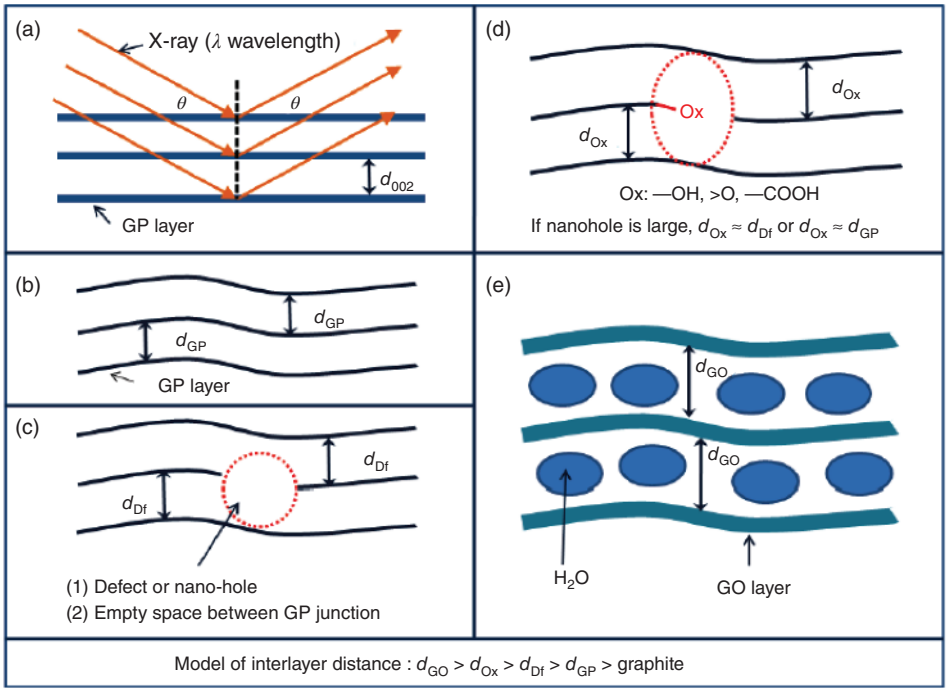

Figure 1.11 Bragg's law for graphene (GP) or graphite (002) planes (a), and models for d_{002} of GO (e), and thermally reduced GP (b–d). In this model, the order of interlayer distance becomes graphite $< d_{GP} < d_{Df} < d_{Ox} < d_{GO}$.

Figure 1.11 [63]. The interlayer distance order is graphite < graphene < defect and nanohole < oxygen bonded functional groups < GO. Particularly, GO has the largest distance about ~5–9 Å because of the inclusion of H_2O between the layers. If defects in the layer are sufficiently large, the space of oxide groups and H_2O molecules can be ignored. Thus, the order could change the distance of (oxygen bonded functional groups) ≈ (defect and nanohole) or (oxygen bonded functional groups) ≈ (graphene). GO has an intermediate structure with oxygen bonded functional groups and defect and nanohole during thermal reduction, and through bottom-up layer stacking, the resultant graphene evolves toward graphite as crystal growth with the removal of gap by oxygen and defects.

In various annealing conditions, GO and graphene films show temperature-dependent XRD patterns. From the change of XRD patterns shown in Figure 1.12, we can figure out that the structure and bonding states of thermally reduced GO depend on the annealing temperature [64]. As increasing temperatures, the (002) peak of a GO film on the left side moves continuously toward the right with a variance in intensity and FWHM as seen from Figure 1.13.

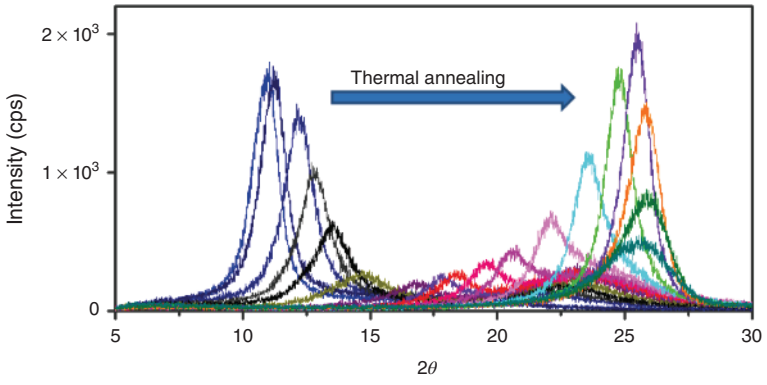

Figure 1.12 Total plot for measured in situ XRD patterns of GO/GP films obtained at room temperature to 1000 °C.

1.3.6
Raman

Raman spectra of GO consists of prominent spectral features, called G at ~1586 cm^{-1}, D bands ~1350 cm^{-1}, and 2D at 2697 cm^{-1}. Raman spectra of all disordered carbons are dominated by the relatively sharp G and D features of the sp^2 sites. The G and 2D peaks represent the E_{2g} vibrational and out-of-plane modes within aromatic carbon rings, respectively. G band is a degenerated optical phonon mode at the Brillouin zone center and is induced by a single-resonance process. The peak near 1350 cm^{-1} is denoted with the D band (in plane carbon ring breathing mode (A_{1g} mode)), which is forbidden in perfect graphite. This process requires a scattering at defect sites in order to conserve the momentum. Previous reports show that the dominant peaks in the D mode spectra originate from phonons between the K and M points of the Brillouin zone. The D mode is dispersive; it varies with photon excitation energy, even when the G peak is not dispersive and its intensity is strictly connected to the presence of sixfold aromatic rings. The G band corresponds to graphite-like sp^2 carbon and D band corresponds to disordered sp^2 carbon induced by the linking with sp^3 carbon atoms. The D peak ultimately gives a relative measure of the amount of sp^3 carbons in the surrounding. Defects such as impurity atoms, functional groups, heptagon–hexagon pairs, folding, and so on, of the graphene layers give rise to the D band. The cooperation between D and G peaks gives rise to a G0 peak near 2931 cm^{-1}.

1.3.7
Photoluminesces (PL) Measurement

Graphene, which is semimetal in nature, the highest occupied molecular orbital (HOMO) and the lowest unoccupied molecular orbital (LUMO) meets in K point, making it a zero band gap material and opening of a band gap can be

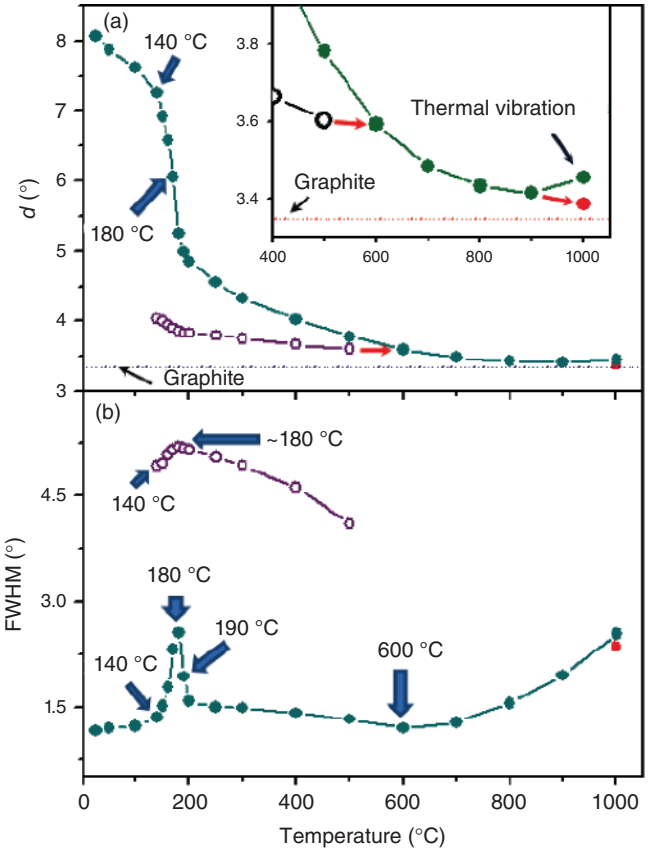

Figure 1.13 FWHM (a) and d_{002} (b) plots for XRD patterns of Figure 1.4. The inset shows a magnified image of (a).

possible due to the functionalization of its lattice with oxygen atom. GO has an electronic structure similar to that of graphene, except for the states near Fermi level and oxygen-related states. The formation of sp^2 clusters in sp^3 matrix is expected to produce quantum confinement effects, which result in an opening of the band gap, at the Fermi level. In graphene, $\pi-\pi^*$ bands degenerate at the K point and coinciding with the Fermi level makes it the zero band gap. But in GO, the π states disappeared near the Fermi level because of bonding between the π and oxygen-related states causing electron transfer from carbon to oxygen and shifting the HOMO state downward results opening of a band gap. Since sigma bands away from the Fermi level and π bands close to it so that the $\pi-\pi^*$ band controls the band gap. Entire π bands lie within the $\sigma-\sigma^*$ gap and the $\pi-\pi^*$ energy states are highly localized due to the large $\sigma-\sigma^*$ gap of the sp^3 matrix. Thus, electron confinement in sp^2 clusters are possible because sp^3 carbon sites act as large repulsive barriers for carrier and thus sp^2 clusters of a smaller size result in larger $\pi-\pi^*$ splitting. Since π and π^* states form the band edge, the size

of the gap depends on the size of the sp^2 clusters and the width of optical gap is found to vary inversely with the sp^2 cluster size. Recombination via emission of photons takes place because electron–hole pairs are localized due to a deep potential well, which separates carriers from extended sigma states.

1.4
Optical Property Modification of Graphene

1.4.1
Absorption Property Modification of Graphene (Terahertz, UV–Visible–NIR)

The optical properties of graphene, GO [65], and rGO shows fairly similar tendency that as GO becomes reduced, it shows properties similar to those of graphene and plasma oxidized graphene (OG) shows what are similar as GO. Therefore, it is significantly essential to figure out tunable transmittance feature for expecting absorbance between graphene and GO with two of treatment, annealing and oxygen plasma (Figure 1.14).

1.4.1.1 Absorption Property of Thermally Annealed Graphene Oxide

Thermal annealing is a very powerful tool to reduce GO. While the chemical method is applicable, still the reduction rate of thermal annealing is the highest. For heating the GO up to 850 °C, most of the oxygen functional groups are reduced and it is shown that only the aromatic rings are still alive. The Raman analysis in Figure 1.15 presents that the GO is reduced by thermal annealing, where its G-peak is shifted to graphene and the D peak increases due to the reduced oxygen atoms. The G-peak shift shows us that the carrier density of GO increases similarly to graphene and that the physical properties of rGO resemble those of graphene. Moreover, when the GO is annealed up to 850 °C,

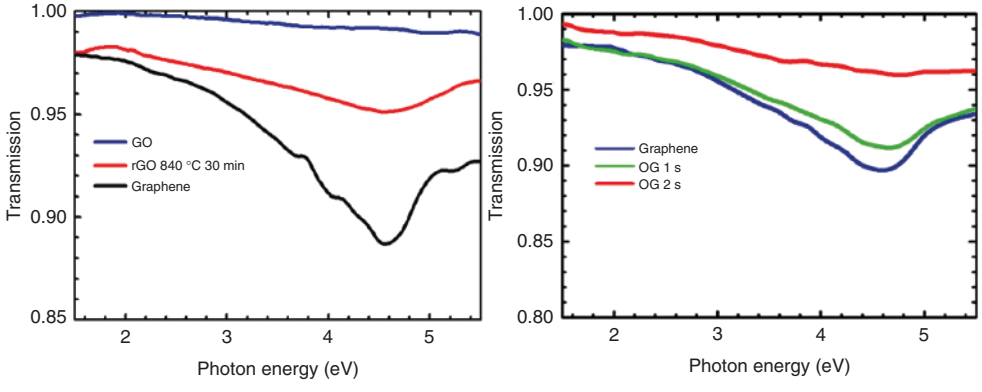

Figure 1.14 Transmission spectrum of graphene and graphene oxide with heat treatment (left) for reduction of GO and Oxygen plasma treatment (right) for making defect and oxidation. OG is equalt to oxygen plasma treated graphene.

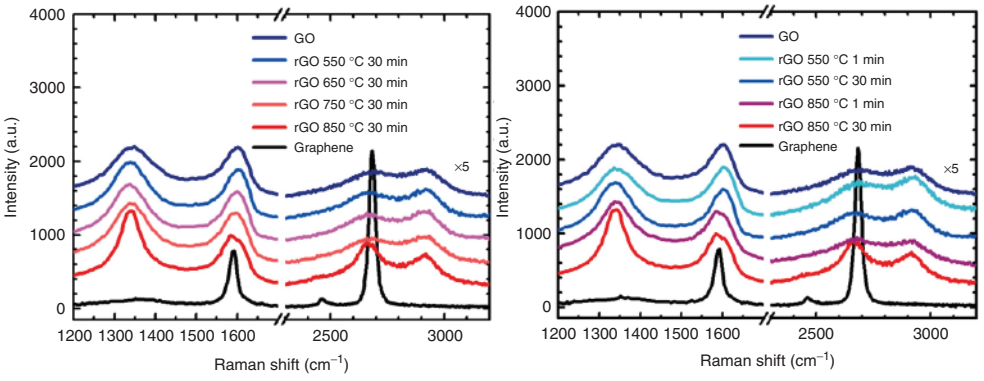

Figure 1.15 Raman spectra of thermally reduced graphene oxide.

the 2D peak dramatically increases, where the crystal structure of graphene is formed by reduction. Also, Raman data show the temperature-dependent, but time-independent reduction of GO.

The ultraviolet (UV)–visible absorption property of thermal rGO in Figure 1.16 shows what similar with the result of Raman spectra. First of all, the monolayer GO and rGO thin films were highly transparent, close to 99%, in the optical range of 1.5–5.5 eV. The transmission of more than 98% at 1.5 eV in rGO is fairly close to the corresponding value of 97.7% in graphene. When the GO is thermally annealed and the annealing rate getting increased, the rGO exhibits lower transmission of 96–98% and a dip in transmission at 4.55 eV. This dip feature at 4.55 eV clearly indicates the restoration of monolayer behavior in rGO as this feature matches the feature in the transmission spectrum of monolayer graphene grown by CVD. This is the same as predicted that the direct inter-band transition in graphene expected at 5.1 eV is smeared out by a strong electron–hole interaction, and the resulting resonant excitonic absorption causes a distinct absorption peak to appear at a redshifted energy of 4.55 eV. Therefore, from the absence and presence of this dip feature in GO and rGO, the restoration of monolayer behavior in rGO has been confirmed. Moreover, the peak for the resonant excitonic absorption becomes stronger and narrower with increasing annealing temperature. A systematic redshift in the absorption peak energy from 4.62 to 4.55 eV is also notable from the absorbance spectra. The 850 °C treatment appears to be the most effective in restoring monolayer-like behavior with its absorption peak energy matching that of monolayer graphene.

1.4.1.2 Absorption Property Plasma Defected Graphene

The oxygen plasma treatment on graphene causes disorder and a doping effect. OG processed by plasma oxidation has several distinct physical properties such as high transparency, low mobility, and a moderate free carrier density [12]. Optical properties in the visible region show the quantized universal absorbance $\pi e^2/\hbar c = 0.023$, where c, e, and $\hbar$ are the speed of light in vacuum, the electronic charge, and the reduced Planck constant, respectively. In the UV

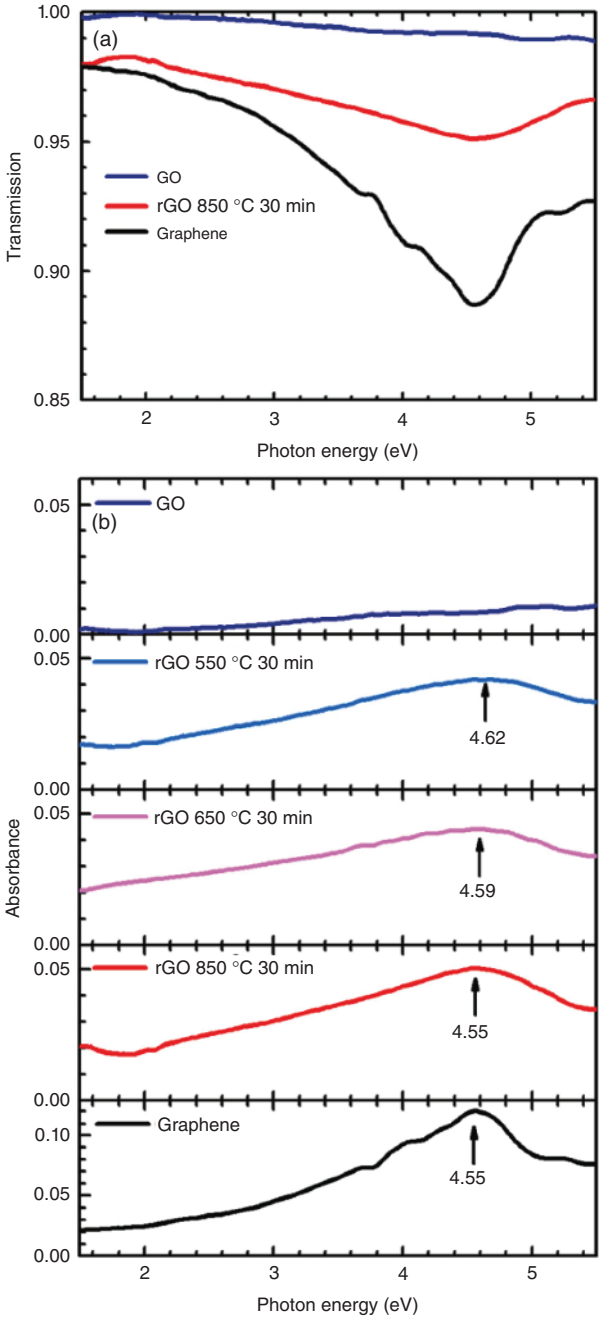

Figure 1.16 (a, b) Visible absorption spectra of thermally reduced graphene oxide.

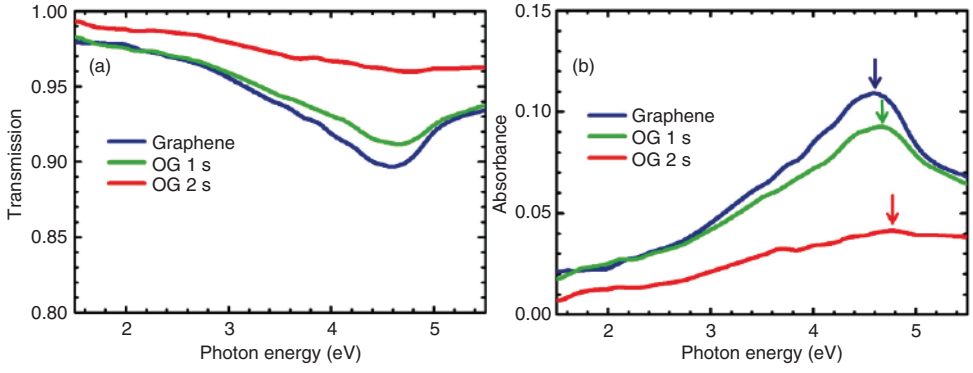

Figure 1.17 The transmission (a) and the absorbance (b) spectra of graphene and oxidized graphene, 1 s oxidization graphene (OG 1 s) and 2 s oxidization graphene (OG 2 s), in the visible and ultraviolet regions.

region, the electron–hole excitonic absorption at around 4.55 eV is one of the main characteristic features of graphene.

In Figure 1.17a, the transmission spectra of graphene and OG in the visible and UV region are compared with the oxidation time. The transmission of OG 1 s is not much different from that of graphene; in contrast, for OG 2 s, the transmission closer to 100% is higher than that of graphene in the visible range. The increase of transmission with the oxidation process is due to a free carrier density decrease and a metal–insulator transition. The result is consistent with the redshift of the Raman G peak and weakened electron–hole excitonic peak resonance in the UV region in Figure 1.17b.

The free carrier dynamics and a metal–insulator transition are well noticed in the terahertz region. Figure 1.18a shows the terahertz time-domain electric field amplitude through vacuum, a fused silica substrate, the graphene film, and the OG films on a fused silica substrate. The time delay compared to that in vacuum

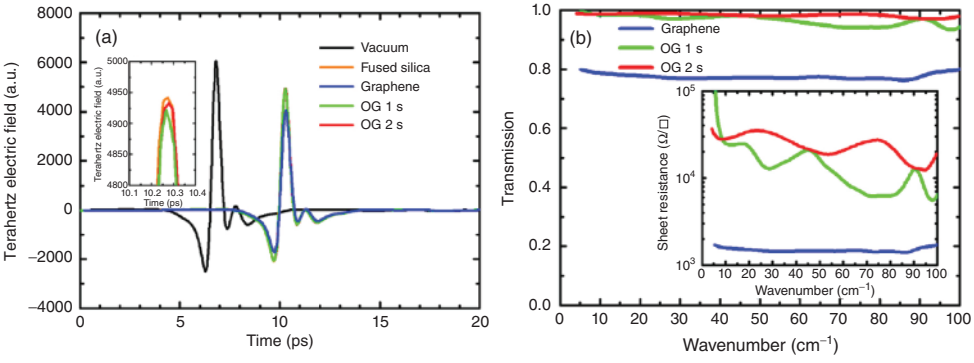

Figure 1.18 Terahertz time-domain electric field (a, main), enlarged terahertz pulse peaks (a, inset), transmission spectra (b, main), and calculated optical sheet resistances (b, inset) of graphene and oxidized graphene in the terahertz region.

is related to their real part of the refractive index and thickness. Furthermore, the terahertz pulse peaks show an amplitude increase due to plasma oxidation. Figure 1.18b shows the transmission spectra (main) and the calculated sheet resistance (inset) of graphene and the OG films. The transmission spectra in the terahertz region shows a free carrier density decrease and again consistent with previous transmission changes in the visible and UV range. The optical sheet resistance $\rho(\omega)$ is obtained from the absorbance $A(\omega) = (4\pi/c)/\rho(\omega)$. The transmission (close 100%) and optical sheet resistance of OG 2 s are higher than those of OG 1 s and of graphene in the terahertz range. The increase in the optical sheet resistance with the oxidation process is again related to a metal–insulator transition. The decrease in the free carrier density directly leads to an increase in DC resistivity. The transparent OG with tunable sheet resistance can be thus conveniently fabricated from our graphene by plasma oxidation, as confirmed by visible–UV and terahertz spectroscopy results.

1.4.2 PL Property Modification of Graphene

1.4.2.1 PL Properties of Oxygen Plasma Treated Graphene

The oxygen plasma treatment to GO causes not only the defect on graphene but also the change in distributions in oxygen functional groups: epoxy to carbonyl. By this physical property modification, the PL spectra becoming redshifted depends on the plasma pressure [66]. Figure 1.19 shows Raman analysis. The GO-1 is pristine GO, and as it becomes GO-4, the oxygen pressure increases. Raman spectra of all disordered carbons are dominated by the relatively sharp G and D features of the sp^2 sites. Also, the G and 2D peaks represent the E_{2g} vibrational and out-of-plane modes within aromatic carbon rings. Due to the oxygen plasma treatment, the intensity of the D peak increases compared to the G peak intensity. The prominent D peak in the Raman spectra is from the structural imperfections created by the attachment of hydroxyl and epoxide groups on the carbon basal plane. This indicates the increased density of structural defects due to oxygen plasma treatment.

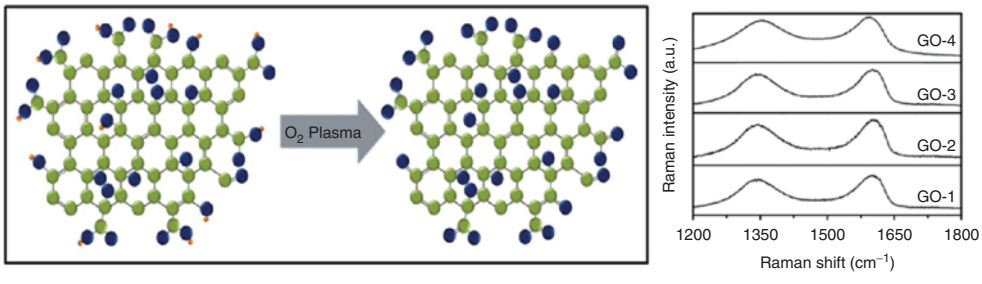

Figure 1.19 Oxygen functional group modification from epoxy to carbonyl and Raman spectra of oxygen plasma–treated graphene oxide dependent to oxygen pressure.

The PL emission spectra of the GO film, showed in Figure 1.20, presents the wavelength of 487 nm where they remain almost constant with plasma treatment with 200 nm excitation. However, as the oxygen plasma treated to GO thin films, the shoulder peak at 530 nm disappears gradually with increasing oxygen pressure (from left to right) and resulting in a much broad emission. The emission intensity of higher wavelength emission (550–650 nm) from the graphene decreases considerably by oxygen plasma treatment.

This results are considerable with the XPS analysis in Figure 1.21 present that it is clear that when oxygen pressure increases sp^3 hybridization increases due to the incorporation of oxygen resulting in O–C–O, C═O, and O–C═C linkage. The epoxy and carbonyl groups usually induce non-radiative recombination of localized electron–hole (e–h) pairs, which leads to the non-emissive property of GO. The oxidation increases reactive sites such as epoxy and carbonyl groups and hence decreases the emission efficiency of the sp^2 domains on GO nanosheets. Moreover, XPS analysis shows that as oxygen pressure increases carbonyl groups increase. For oxygen-treated films it can be inferred that due to the presence of an increased number of carbonyl groups, most of the electrons excited to the high levels relax non-radiatively, which decreases the PL emission in higher wavelength region. Moreover, for these samples, the nonuniformity of graphene edges and the potential for dangling bonds are thought to have significant influence on their chemical properties and reactivity, which may also decrease the PL emission in the higher wavelength region.

1.4.2.2 Substrate Effect

Optical and structural properties of GO are varied with the changes of substrates. Substrates significantly influence the properties because the interaction between substrate and GO modifies the electron band structure [19]. Graphene is semimetallic since its HOMO and LUMO are in contact, resulting in the zero band gap material [67]. However, graphene on a SiC substrate shows a band gap of around 0.26 eV possibly due to the interaction of a substrate. The presence of oxygen-related functional groups increases the possibility of reactivity. If graphene and their substrates have interactions yield band gap then its applications in transistor or optoelectronic devices could considered due modified band structures. In this section, we will compare four types of fabricated devices; G1 for GO/Au NPs/quartz, G2 for GO/ITO/glass (indium tin oxide), G3 for GO/quartz, and G4 for GO/SiO_2/Si. We can confirm that GO has different types of oxygen-related functional groups by EELS analysis. The peak at 285 eV reveals that the 1s for carbon to the π^* state transition exists in the range of carbon K-edge spectrum, and the peak at 291 eV represents 1s for carbon to the σ^* state transition within the same ranges. The peak of 539.7 eV within the range of oxygen K-edge spectrum means that higher-order π^* resonance of every oxygen and σ^* resonance of the 1,2-epoxy linkage exist [68]. Around 200 nm absorption peak of UV–visible are exhibited on every sample corresponding to $\pi-\pi^*$ transition attributed to carbon bonding in aromatic sp^2 clusters. There are some variations of UV–visible spectra in all samples due to changes of linkages with epoxide and

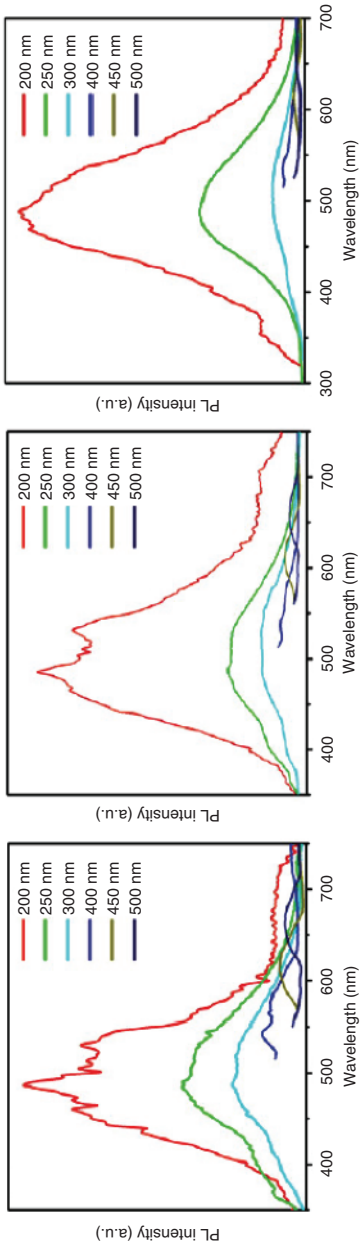

Figure 1.20 Oxygen plasma–dependent PL property modification of graphene oxide.

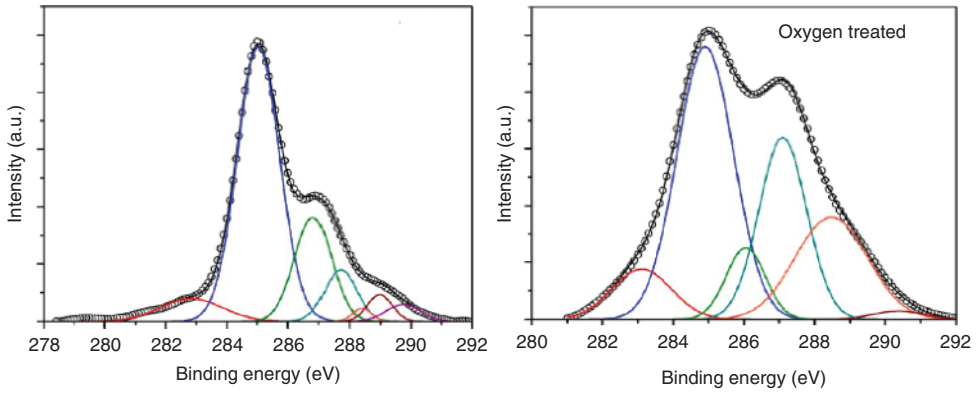

Figure 1.21 XPS analysis of graphene oxide with oxygen plasma treatment.

peroxide. There is an extra peak around 420 nm with the G1 because gold NP generates surface plasmon resonance affecting additional absorption. Also, G1 shows almost a constant value of absorption in the whole visible range. Therefore, substrates are enough influential to the absorption value, which correspond to the band gap. G2 shows almost absent value of Fourier transform infrared (FTIR) peak around 1600 cm^{-1} for carboxyl group vibration and 1726 cm^{-1} for C═O stretching vibration related to carbonyl and carboxyl groups [69]. Compared to normal GO having ~10.5° ($d = 0.83$ nm) measured by XRD, G2 shows 24° ($d = 0.36$ nm) due to a low number of oxygen functional groups, while G4 has a peak of 11.26° ($d = 0.789$ nm) originated from the diffraction plane (002) in agreement with the FTIR spectrum [63]. Also, the D band of Raman shift can present oxygen functionalities in different films because of the band related with oxygen content in GO. Gold NPs act as a hot spot generating localized surface plasmon polariton, which leads to the changes of lattice parameter resulting in shift of G and D bands. The XPS spectrum specified with C1s shows how much oxygen functionalities exist in the films. As of the same results of the previous measurement, G2 shows the lowest peak ratio of 286.2 eV for O–H/O–C–O and 288.4 eV for C═O since oxygen atoms are transferred from GO to ITO. Also, the indium XPS spectrum shows that the peak for $3d_{5/2}$ moves higher after treated with oxygen plasma (443.7 – 444.02 eV) and the results of shift happens with respect to the work functions. Thus, GO is reduced when it is deposited on ITO substrates. G3 shows a lower intensity value of peak at around 286.2 eV for O–C–O than G1 and G4 because the number of epoxide linkage is small. In the XPS of G1, there are additional peaks; 285.4 eV for defected sp^2 and 283.9 eV for Au–C hybrid bond. The defected peak position affects the overall peak of XPS in binding energy according to carbon atoms out of sp^2 configuration. Thus, gold NP makes delocalized bond to localize in it, resulting in the disorder of sp^3. Since GO is composed of sp^2 clusters in sp^3 matrix, quantum confinement opens the band gap at the K-point. This is related to the oxygen functionalities that make the HOMO levels lower. Those samples show similar PL peaks of 495, 540, and

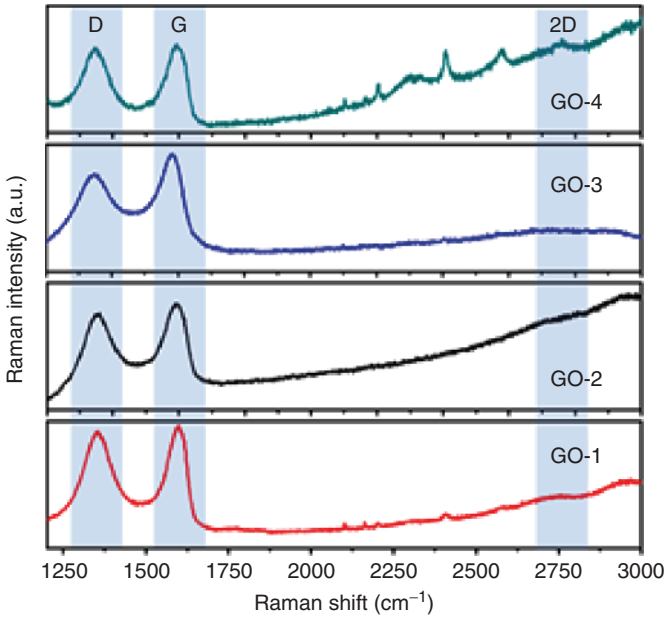

Figure 1.22 Raman spectra of graphene oxide films (GO-1, GO-2, GO-3, and GO-4).

650 nm corresponding to the size of clusters (1.2, 1.3, and 1.4 nm, respectively). For getting information for the substrate effect on Raman spectra, Raman analysis of GO films coated on different substrates are presented in Figure 1.22. The films are named as GO-1 (GO/Au/quartz), GO-2 (GO/ITO/glass), GO-3 (GO/quartz), and GO-4 (GO/SiO_2/Si). GO-2, GO-3, and GO-4 films show spectral features, called G around 1590 cm^{-1}, D ~1350 cm^{-1}, and 2D at ~2697 cm^{-1}. But for GO-1 (GO/Au/quartz) film G band, D band, and 2D band positions are found to be 1579, 1339, and 2709 cm^{-1}, respectively. G band, G0, and 2D band positions are almost constant for GO-2, GO-3, and GO-4 films with a slight variation in D band nature. Since D band depends on the oxygen content in GO, this could be due to the changes in oxygen functionalities in different films. But for GO-1 (GO/Au/quartz) film G band, D band, and 2D band positions vary strongly compared to other films. The changes in these band positions are interpreted as the local field enhancement in the nanostructure of the gold-coated quartz substrate. There is a possibility of the generation of local field at the contact areas of the two structures by coupling the localized surface plasmon of the gold NPs with the surface plasmon polariton of the graphene film, which leads to the changes in the graphene lattice parameter with the corresponding G and D peak shifts. The graphene–gold bond is covalent in nature; such bonding would change its lattice constant as well as the electronic properties. Also, there is a possibility that the lattice mismatch between the graphene lattice and the interfacial gold layer may cause a compressive stress on graphene; hence the shift of the G band Raman peak frequencies. The

relation introduced for point-like defects in nanocrystalline graphene established that I_D/I_G varies inversely with the distance of an average distance between defects (L_D) $\frac{I_D}{I_G} = \frac{C(\lambda)}{L_D^2}$. Where, C is variable depend on wavelength. With an increase of the ID/IG ratio, there is an increase of the crystallite boundaries and a reduction of the crystallite size. But Ferrari reported that Tuinstra–Koenig relation is not valid above a critical defect density where the cluster size (La) of sp^2 is smaller than 2 nm; the ID/IG ratio increases with the number of aromatic rings, opposite to what is expected from the Tuinstra–Koenig Relation. For La below about 2 nm, they proposed a second amorphization stage and according to the phenomenological model for this stage, the ratio decreases as the crystallite size is reduced: $ID/IG = C'La^2$, where $C = 0.0055$ and La in angstroms. In the first stage, the increase of the ID/IG ratio indicates an increase in the disorder, while in the second stage, the increase of the ID/IG ratio indicates a decrease in the disorder.

A different size of cluster shows different PL emission because the amount of delocalized orbital. G1 shows different dominant peak positions of 435 and 450 nm. The d orbital of Au and π orbital of aromatic carbon has interactions, effecting on defected sp^2 hybridized carbon atoms of band structure. The interaction modifies the band structures related with Fermi level, electron phonon coupling. Thus, GO films on different substrates vary the optoelectronic properties such as PL and absorption related with band structures. The substrates affect tremendously the structural and optical properties such as interlayer spacing, sp^2 cluster confinement changes, and band structure. The blueshift of PL emission is shown in gold buffers between GO and the substrate with respect to generating defected sp^2 sites. The luminescence emission of films at various excitations ranging from 200 to 450 nm for GO films coated on different substrates are shown in Figure 1.23 and inset of Figure 1.23c shows emission from GO solution. The films are named as GO-1 (GO/Au/quartz), GO-2 (GO/ITO/glass), GO-3 (GO/quartz), and GO-4 ($GO/SiO_2/Si$). Figure 1.22 shows the emission from substrates (Au/quartz, ITO/glass, SiO_2, quartz), which is also shown for reference.

The schematic representations of band level diagram of corresponding films are shown in Figure 1.24. GO-2, GO-3, and GO-4 ($GO/SiO_2/Si$) films show almost a similar PL emission behavior with the peak emission corresponding to around 495 nm (2.5 eV marked as γ), 540 nm emission (around 2.3 eV, marked as δ), and 650 nm emission (around 1.9 eV, marked as ϕ) in Figure 1.24a,b. In addition to these emissions, the GO-1 (GO/Au/quartz) film shows emission peaks around 435 nm (2.83 eV, marked as α), 450 nm (2.74 eV, marked as β), and 580 nm (2.13 eV, marked ε) in Figure 1.24d,e,f. The average cluster size of around 1.2 nm corresponds to an emission around 495 nm (2.5 eV marked as γ); the larger clusters (1.3 nm) give 540 nm emission (around 2.3 eV, marked as δ) and much larger clusters (1.4 nm) result 650 nm emission (around 1.9 eV, marked as ϕ) in Figure 1.24a and 3.11b. Emissions around 425 and 350 nm correspond to emission from substrate (marked as "s" in Figure 1.24a). sp^2 clusters of different size ranges release excitation-dependent emission. At 200 nm excitation, emissions from all clusters are observed resulting in a broad emission ranging from 400 to 600 nm. However,

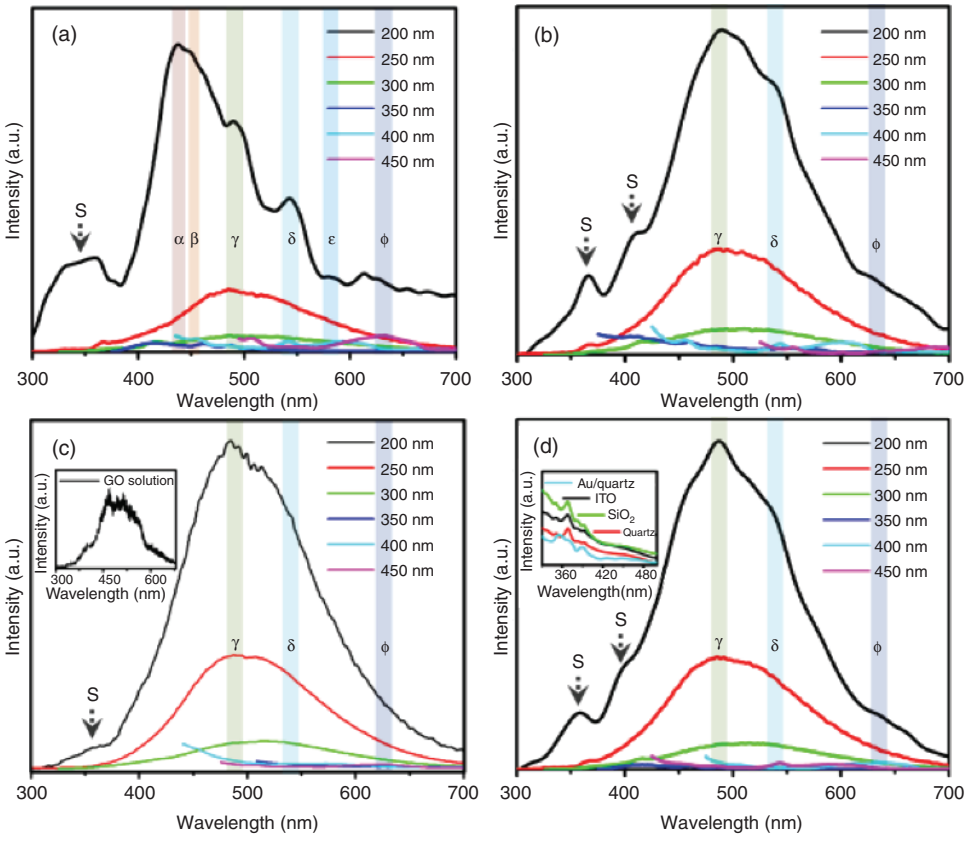

Figure 1.23 PL spectra of graphene oxide films (a) GO-1, (b) GO-2, (c) GO-3, and (d) GO-4 showing excitation-dependent PL emission. Inset of (c) shows emission from GO solution, Inset of (d) shows emission from substrates (Au/quartz, ITO/glass, SiO_2, quartz).

when excited using higher wavelength, radiation emission from selected clusters (large clusters) are only observed. This may be the reason for reduction of PL emission intensity in higher excitation wavelengths. Attractive interaction between the d-orbital's of gold atoms and the π-orbital of the sp^2-hybridized carbon atoms can create some defected sp^2 levels, which results in some additional localized energy level in π*, which accounts for the variation in PL emission when compared to other films. In the Au/quartz film, the observed peaks in Figure 1.24a are around 435 nm (2.83 eV, marked as α), 450 nm (2.74 eV, marked as β), 495 nm (2.5 eV, marked as γ), 540 nm (2.3 eV, marked as δ), 580 nm (2.13 eV, marked as ε), and 650 nm (1.9 eV, marked as ϕ). These transitions are shown in Figure 1.24b.

1.4.2.3 Pd Grafted Graphene Oxide

In order to apply graphene for the application of electronic and optoelectronic devices, graphene overcomes its limitations attributed from the lack of a band gap.

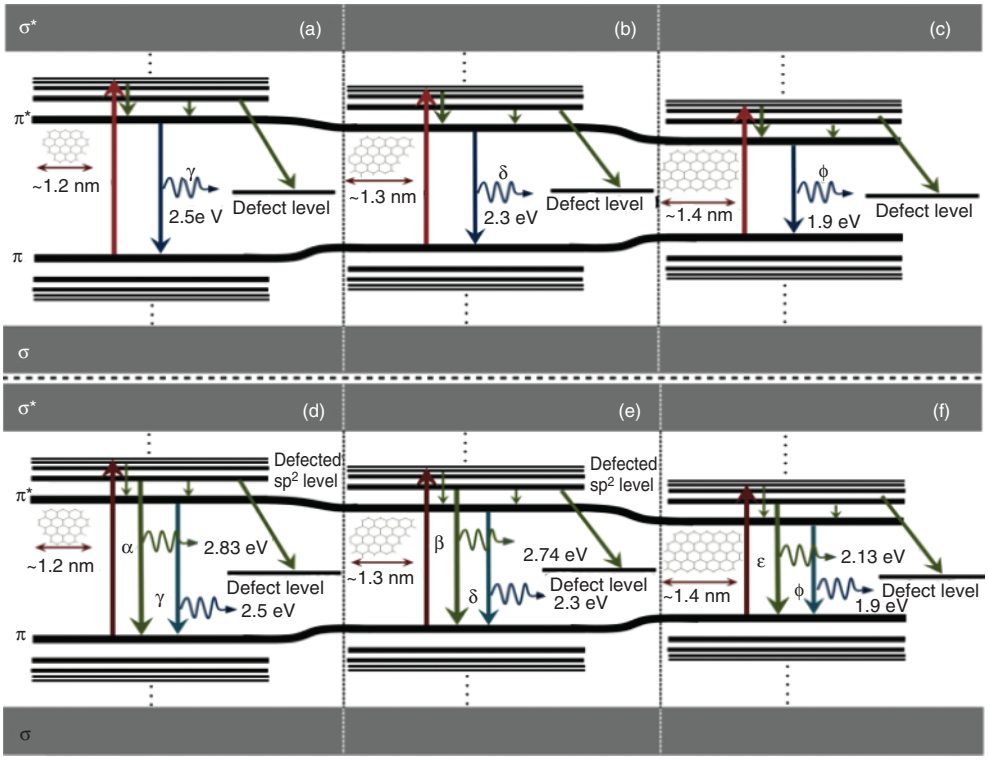

Figure 1.24 (a–f) Schematic representation of band level diagram of GO for GO-1, GO-2, GO-3, and GO-4 films.

As modification methods, many research groups have been studying optoelectronic properties of GO functionalized with NPs of metal or semiconductors such as TiO_2, Co_3O_4, Pt, Pd, Ag, and Au. Various application fields including optics, electronics, catalysis, and sensors are adopted graphene-based matrix mixed with NPs mentioned above. Confined electrons in localized sp^2 orbital affect the optical properties of GO such as optical absorptions and broadband fluorescence in the spectral region from UV to near infrared. Remarkable physical and chemical properties of palladium and palladium oxide attract tremendous attention in transition metal and metal oxide dopant application respectively. Particularly, applications in sensors and optoelectronic devices are possible because of its catalytic properties as well as the composite structure of graphene-supported palladium [13]. Similar spacing in both carbon aromatic structure in graphene (0.246 nm) and interlayer of palladium (0.225 nm) is evidence that composite structure is possible. Palladium grafting affects photoluminescent property since it regulates the reduction of GO. Pristine GO has more structural defects than GO and rGO is obtained from bonding with oxygen and carbon atoms, transforming orbital to sp^3. EELS shows that the absorption peak of 536.7 eV is detected due to the resonance of epoxide bond, which appears to be σ^*

and higher-order π*. Ungrafted GO emits yellow-green PL from defect-trapped excitons. As the annealing process progressed, the restoration rate increased resulting in the decrease of yellow-green PL and increase of blue PL. FTIR spectra of GO shows that decrease of peak (1730 cm^{-1}) correspond to carbon and oxygen double bonds with respect to annealing. The sp^2 site originating blue PL emission increases when GO is reduced. The annealing process, that is, thermal heating in low pressure Ar environment condition results in the elimination of functional groups; as a consequence, sp^3 transforms to sp^2 clusters. The role of palladium decorating GO for PL emission was investigated, and various measurement techniques were used to analyze the origin of PL emission. Palladium enhances the probability of reduction since palladium acts as a reducing agent, increasing the C═C–C aromatic ring vibration. Also, sp^2 fractions are enhanced compared to pristine GO due to the synthesis of palladium oxide, and further annealing affects strongly the increase of the restoration rate related to the blue PL emission. The tailoring effects of palladium are confirmed with various measurement techniques such as XPS, Raman, EELS, UV–visible absorption, FTIR, and so on. Compared to interplanar distance of pristine GO, palladium grafted GO shows a larger value of lattice spacing due to the presence of palladium identified as (002) reflections. Transitions from the 1s to σ* due to palladium changes peak position of EELS corresponding to the carbon K-edge region, and palladium generates a peak of its M 4,5 edge. The peak intensity of FTIR shows that positions of 1050, 1100, and 1200 cm^{-1} correspond to a single bond of carbons, single bond of carbon and oxygen, and C–O–C stretching vibration respectively are equally dominant before annealing in grafted samples. As annealing temperature increases, C–C stretching vibration peak (1050 cm^{-1}) gets intensive. In the case of ungrafted GO, it also shows similar tendency of peak intensity in annealing, but dominant intensity increase rate is lower than grafted GO. With the XPS spectrum, carbon and oxygen-related functional groups of GO can be detected clearly. Since the aromatic bonding of carbon is dominant, the most intensive peak is positioned at 284.6 eV rather than any other peaks such as 286.2 eV for O–H/O–C–O, 287.8 eV for C═O, 288.5 eV for O–C═O, and 289.3 eV for carboxyl group. Thus, as the annealing temperature increases, the relative intensity of 284.8 eV increases because of restoration in sp^2 clusters from sp^3 sites. Comparing both pristine and grafted GO with the XPS spectrum, the restoration rate of palladium grafted GO is higher than pristine GO. In agreement with the above measurement, UV–visible absorption shows broad peaks related to the π–π* transition in various sized clusters of sp^2 ranging from 240 to 260 nm. Also, the range of 295–305 nm related to n to π transition with respect to the linkage of epoxide (C–O–C) and peroxide (R–O–O–R). Also, the overall range of visible absorption is enhanced as sp^2 clusters increases with respect to reduction, and grafted GO shows that it absorbs a visible range relatively more than pristine GO. Thus, we can infer that palladium acts as a reducing agent. The conjugation electron within the GO increases as oxygen extracted from functional groups, resulting in the restoration of aromatic sp^2. Since palladium grafting affects the alternation of bonding alternating between single and double bond of carbon

within the sp^2 network, palladium-grafted samples show extra peaks related to the combination modes of phonons for in-plane transverse optical (iTO) and in-plane transverse acoustic (iTA) around K-point (2300 cm^{-1}) and an overtone away from the K-point (2400 cm^{-1}). With those investigations, the structural changes are demonstrated, and effects on band structures are strongly related with PL emissions. Palladium on GO sheets tailors photoluminescent property and annealing effects, which also related to PL emission. The area of sp^2 clusters increases related to the $\sigma-\sigma^*$ band when palladium is decorated on GO. PL peaks are emitted around 465 and 485 nm are enhanced when palladium is grafted on increasing the annealing temperature. With the results of XPS, Raman, UV–visible investigations, we can infer that those blue PL (465 and 485 nm) is attributed to sp^2 clusters with an area of a different size. Also, the decrease of yellow-green emission with reduction reveals that the peak is originated from the defect site. Moreover, the quenching effect is stronger when palladium is grafted on GO. The PL emission (Figure 1.25) consists of peaks around 465, 485, 505, and 536 nm. All films (GOPd and GO) show the peak emission around 465 nm (~2.66 eV marked as α) and 485 nm (2.5 eV marked as β), attributed to radiative recombination of electron–hole pairs (e–h pairs) generated within localized $\pi-\pi^*$ states (schematically shown in Figure 1.26).

Peak emission around 505 nm (2.44 eV, marked as γ) and 530 nm (2.32 eV, marked as δ) corresponds to emission from defect states due to oxygen functionalities as schematically shown in Figure 1.26a–e. The presence of oxygen functionalities may give rise to defect states in the $\pi-\pi^*$ gap. Thus, in GOPd and GO films, the γ and δ peak emission intensity get reduced with the annealing temperature. With annealing, defect density reduces due to the removal of oxygen functionalities and thereby reducing the intensity of γ and δ peaks (Figure 1.25b). Also PL emission intensity from annealed GOPd films (GOPd-3 and GOPd-4) is lower when compared to annealed GO films (GO-3 and GO-4). This could be

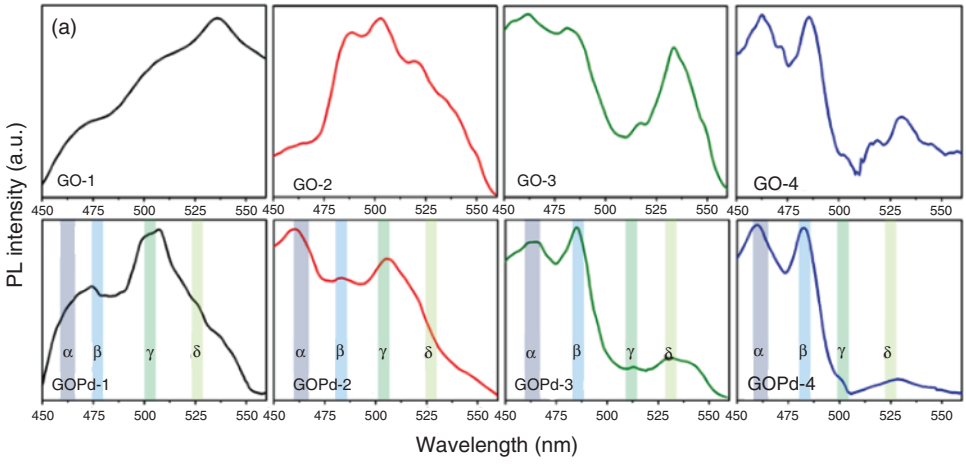

Figure 1.25 PL emission spectra of (a) Pd grafted and (b) ungrafted GO films.

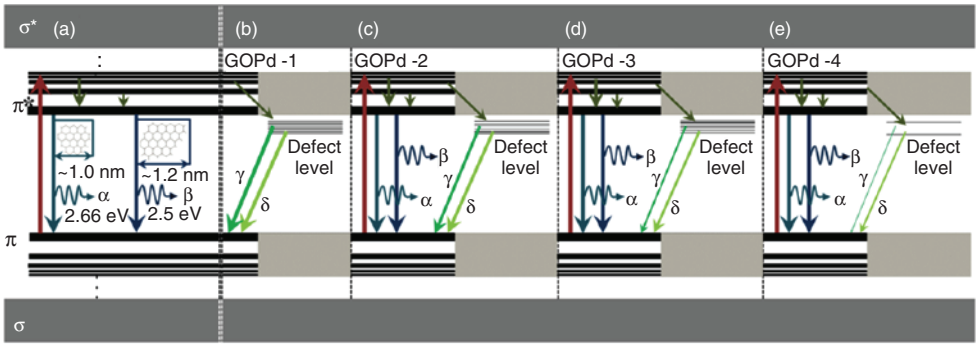

Figure 1.26 (a–e) Schematic representation of band level diagram of GOPd films.

due to the decrease in defect density in GOPd films compared to GO films. As reduction of GO increased (GOPd-4), yellow-green emission (γ, δ) decreased and blue PL became the prominent emission. Since the restoration of electronic conjugation is happening in graphene with reduction, the blue PL emission is expected to originate from sp^2 clusters and the yellow-green PL from trapped states. Irregular PL spectra suggest that trapped states influence the emission spectra. In GOPd film, with annealing temperature, the blue emission is enhanced while the green-yellow emission intensity is reduced. Even though the quenching of green-yellow emission was also observed in ungrafted films, quenching was more prominent in annealed grafted films.

1.5 Optoelectric Application of Graphene

Massless electrons behave as Dirac fermions, with a linear energy–momentum relation [70–72], on the bi-dimensional structure of graphene. As a result, electronic properties of graphene is arisen from a two-dimensional gas of charged particles derived by the relativistic Dirac equation. Carriers mimicking particles are with zero effective mass and the Fermi velocity of electron is $10^6\,m\,s^{-1}$ [71, 72]. The mobilities of graphene, up to $10^6\,cm^2\,V^{-1}\,s^{-1}$, are reported in suspended samples. Graphene is a potential material for nanoelectronics, particularly high frequency, by combining with near-ballistic transport at normal ambience [73].

Graphene also exhibits extraordinary optical properties. It can be transparent although being a single atom level thickness [74, 15, 75]. The linear dispersion relationship with Dirac electrons leads widespread applications in photonics. Saturable absorption is a remarkable characteristic of graphene as a consequence of Pauli blocking [76]. Nonequilibrium carriers in graphene cause hot luminescence [77]. Graphene can also produce the PL by chemical and mechanical treatment. Graphene is a prime candidates for photonic and optoelectronic applications

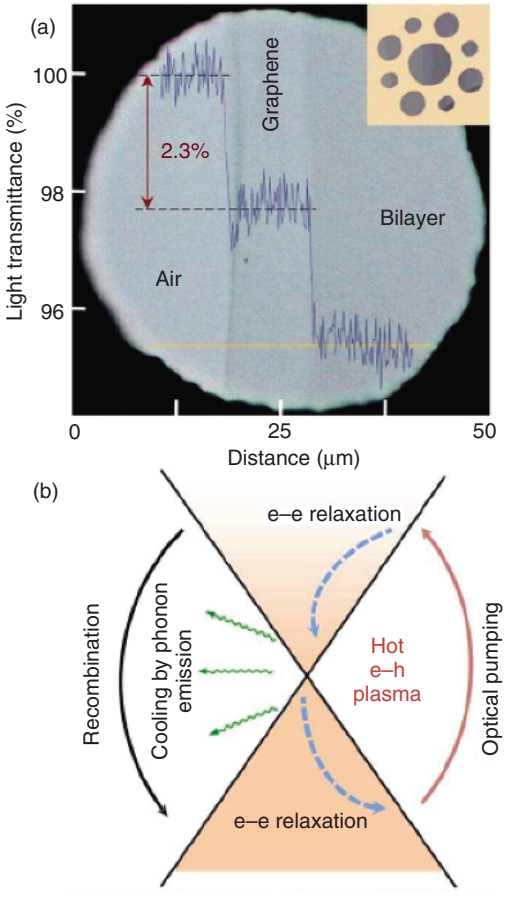

Figure 1.27 (a, b) Transmittance for increasing number of layers. Schematic of photoexcited electron kinetics in graphene, with possible relaxation mechanisms for the nonequilibrium electron population.

thanks to unique physical properties such as light transmittance and small band gap with dirac point [21, 78] (Figure 1.27).

Low-sheet resistance R_s and high transparency is required for optoelectronic devices such as displays, touch screens, light-emitting diodes, solar cells. For a rectangle of length L and width W, the resistance R is:

$$R = \frac{\rho}{d} \times \frac{L}{W} = R_s \times \frac{L}{W}$$

In a thin film $R_s = \rho/d$, where d is the film thickness and $\rho = 1/\sigma_{dc}$ is the resistivity. The number of squares of side W that can be covered on the resistor without overlapping can be seen as the term L/W.

Semiconductor-based transparent materials [79] for electrode are various: zinc oxide (ZnO) [80], doped indium oxide (In_2O_3) [81], tin oxide (SnO_2) [79], as well

as ternary compounds based on their combinations. The most famous material is a doped n-type semiconductor composed of In_2O_3 and SnO_2 with 9 : 1 proportion, called *indium tin oxide* (*ITO*) [79]. The impurities as Sn atoms acting as n-type donors effect on the electrical and optical properties of ITO considerably. ITO has ~80% transmittance and R_s as low as $10\,\Omega\,\text{sq.}^{-1}$ on glass, and $\sim 60-300\,\Omega\,\text{sq.}^{-1}$ on polyethylene terephthalate (PET) [82]. ITO undergoes critical limitations with cost from scarcity of Indium, processing requirements, difficulties in pattering, sensitivity to acidic and basic environments [79, 82]. Also, ITO is brittle and weak at external impulse; in addition, it can easily wear out if it is bending such as touch screens and flexible displays. For overcoming the disadvantages of ITO, metal grids [83], metallic nanowires [84], and other metal oxides [81–84] have been studied. Graphene and graphene-based materials exhibit the considerable performance for transparent conductor. Graphene films show much higher transmittance and wider useful wavelength range than single-wall carbon nanotube films, thin metallic films and ITO. In Figure 1.28, compared to several transparent conductor materials, transmittance and sheet resistance is described. The graphene is more transparent than any other materials for the widespread wavelength range. Sheet resistance is also lower and better than ITO, nanotube, and Ag nanowire mesh.

A photovoltaic device concerned with the solar cell, photo detector transfer energy from light to electricity [85]. The efficiency of energy conversion is defined by the ratio of maximum and incident power, $\eta = P_{max}/P_{in}$, where P_{max} is determined by voltage and current in circuit. Silicon with η up to ~25% is the dominant material for photovoltaic device [85, 86]. The use of polymers in Polymer-based organic photovoltaic cells is for light absorption with efficient charge transport. Even though polymer cells have lower η, they have the advantage of manufacturing economically compared to Si cells by a roll-to-roll process [87]. An organic photovoltaic cell is a transparent conductor used for a photoactive layer and the electrode. Dye-sensitized solar cells consist of a liquid electrolyte as a charge transport medium. As incoming light from outside, the dye molecules absorb the incident photon producing electron–holes pairs. The electrons are transported to the cathode. Dye molecules regenerate by absorbing electrons from a liquid electrolyte. Current the most well-known material is ITO used as photoanode and cathode with Pt coating. The optical properties of graphene can satisfy the requirements for photovoltaic devices. First, graphene is a transparent conductor, which is beneficial for window. Second, graphene is photoactive material due to unique dispersion relation between energy and momentum. Moreover, graphene has very high mobility and low effective mass of electron for charge transport. Lastly, graphene has a catalytic character to other material for fast interaction. The various photovoltaic device applications such as inorganic, organic, and dye-sensitized solar cell, organic light emitting device (OLED), photodetector are shown in Figure 1.29.

Electroluminescent material is needed for organic light-emitting device between two charge-injecting electrodes, and at least one of which is transparent [88]. The HOMO and the LUMO capture the hole and electron at the anode and cathode. This capturing process is connected to matching the work function

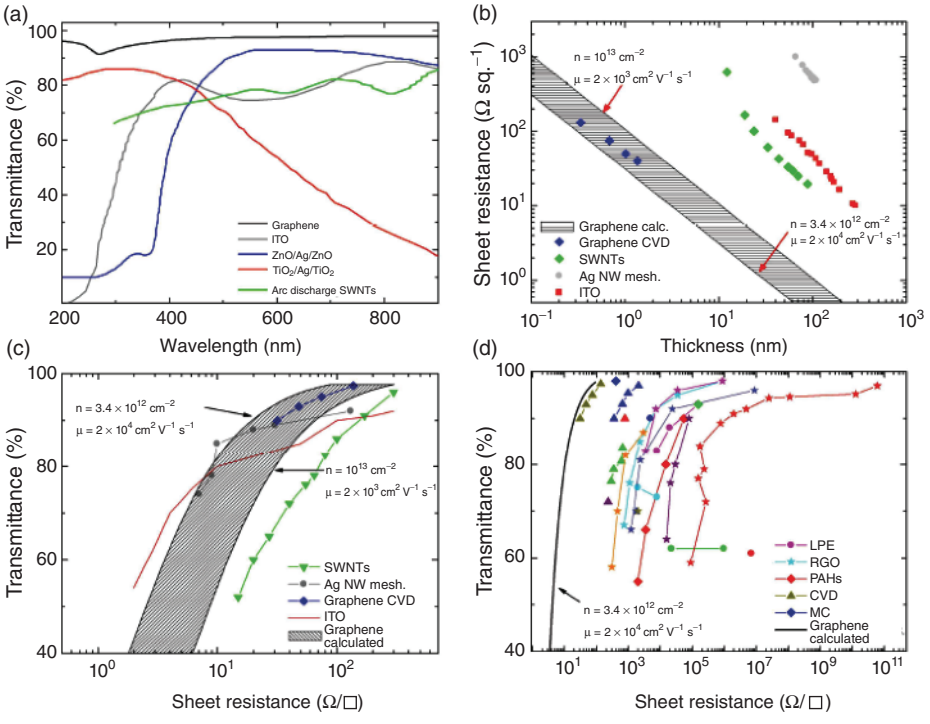

Figure 1.28 (a) Transmittance for different transparent conductors: GTCFs (Graphene-based transparent conductive film) 37, single wall carbon nanotubes (SWNTs) 73, ITO74, ZnO-Ag-ZnO75, TiO_2/Ag/TiO_2 76, where Agis silver and TiO_2 is titanium dioxide. (b) Thickness dependence of R_s blue rhombuses, roll to roll GTCFs37; red squares, ITO74; gray dots, metal wires74; green rhombuses, SWNT73. Two limiting lines for GTCFs are also plotted (hatched area), using typical values for n and μ. (c) Transmittance versus R_s for different transparent conductors: blue rhombuses, roll to roll GTCFs37; red line, ITO74; gray dot, metal wires74; green triangles, SWNTs73. Hatched area, limiting lines for GTCFs calculated using n and μ as in (b). (d) Transmittance versus R_s for GTCFs grouped according to production strategies: CVD35–37,77, micromechanical cleavage (MC)78, organic synthesis68, LPE (liquid-phase exfoliation) of pristine graphene42,43,47,78 or GO52,54,79–81. A theoretical line as for Equation 8 is also plotted for comparison.

of the anode and cathode. OLED have been explored a number of applications in ultrathin television and other display screens, for example, the monitor of computer and mobile phone. Because organic light-emitting devices have advantage of the low power consumption, high image quality and are possible to manufacturing ultrathin device. Similarly in other applications, ITO with 4.4–4.5 eV is mainly exploited material for display even though it has several limitations such as mechanical property, since ITO is brittle, and limited bending and cost issue [89]. Moreover, ITO has a tendency of diffusing into the active OLED layers, which result in a decline of performance over time. The graphene

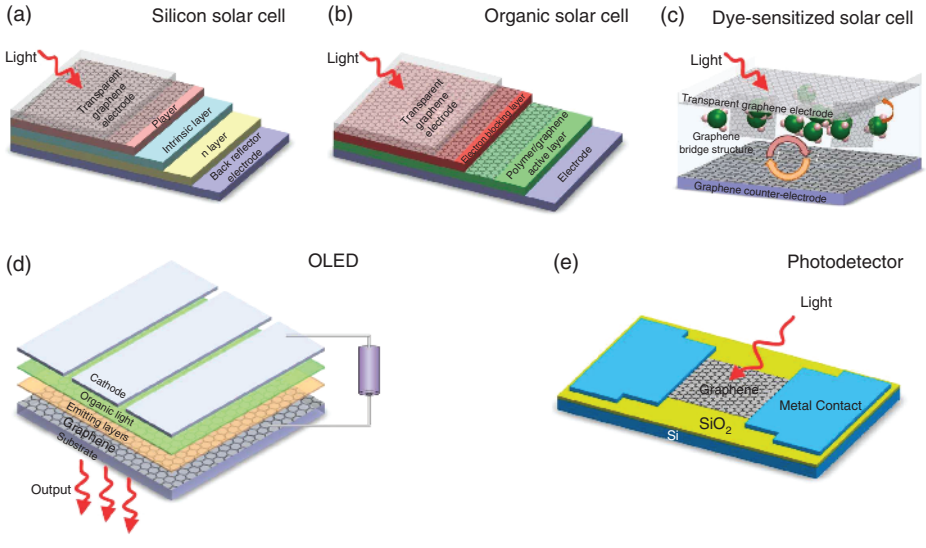

Figure 1.29 Schematic representation of (a) inorganic,(b) organic, and (c) dye-sensitized solar cell, (d) organic light emitting device (OLED), and (e) photodetector.

can alter ITO with 4.5 eV work function and easy to obtain as well as flexible mechanical property included in graphene. Figure 1.30 shows the expected OLED design with graphene without the diffusion problem.

The photodetective device measured photon flux or optical power by transferring the absorbed photon energy into electricity. Photodetectors has copious applications such as remote controls, DVD players, and so on [90]. The excited electrons by photon energy move from the valence to conduction band and electron–hole carries generate the electric current. The band gap limits absorption of light over broad wavelength range because the light with long-wavelength and low quantum energy cannot excite the electron. The graphene can deal with the light from UV to terahertz [91, 92]. Consequently, photodetector made of graphene could work through extensive range of wavelength. Furthermore, the response time of graphene is promising due to great mobility with zero effective mass.

Nonlinear optical and electro-optical properties are necessary for most photonic applications [93]. Laser manufacturers with laser sources providing nano- to sub-picosecond pulses handle with basic research, material processing, circuit board printing, as well as metrology and even eye surgery, and so on. Mode-locking is the most important technique of ultrafast laser systems, which needs the nonlinear optical elements, called *saturable absorber*. Saturable absorber converts the continuous wave beam into a sequence of ultrafast optical pulses [94]. The nonlinear materials require fast response time, strong nonlinearity, and wide useful wavelength range. In addition, in terms of manufacturer, the advantages are high-power handling, low-power consumption, cheap and easy ways of setting up the optical system. Presently, the dominant material of saturable absorber is made

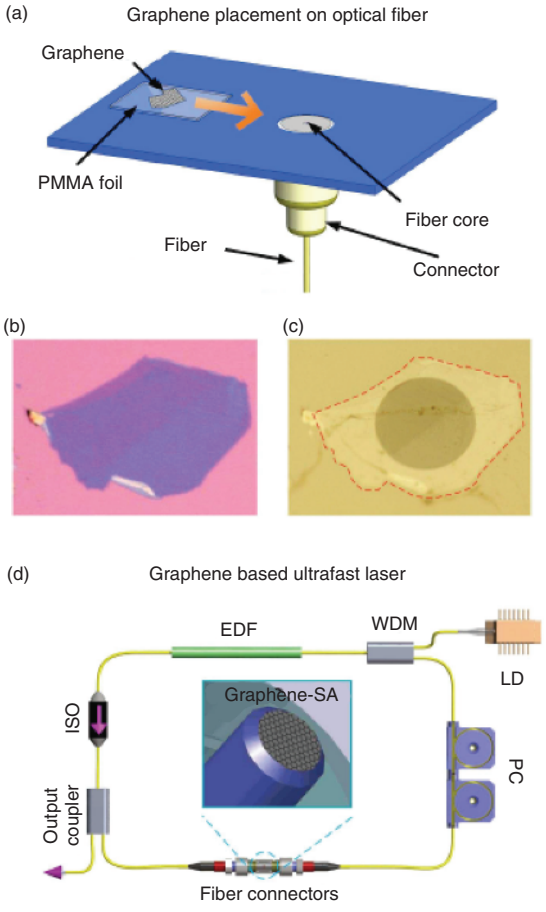

Figure 1.30 (a) An optical fiber is mounted onto a holder. Once detached from the original substrate, a polymer/graphene membrane is slid and aligned with the fiber core. (b) Flake originally deposited on SiO_2/Si. (c) The same flake after deterministic placement. (d) Graphene-mode locked ultrafast laser: a graphene saturable absorber is placed between two fiber connectors. An Erbium doped fiber (EDF) is the gain medium, pumped by a laser diode (LD) via a wavelength-division-multiplexer (WDM). An isolator (ISO) maintains unidirectional operation. A polarization controller (PC) optimizes mode-locking.

by semiconductor saturable absorber mirror. However, it has the disadvantages of tuning range, fabrication and packaging. First, single-wall nanotube was trying to replace the earlier material with low cost and possibility of operating wavelength by controlling of diameter [95]. Graphene can solve the problems of traditional materials (such as Silicon, CNTs etc.,) for the following reasons: Graphene has no restriction of operating wavelength and ultrafast carrier momentum. Compared to conventional materials with mirror or nanotube, it is not necessary to consider the band gap.

References

1. Schedin, F. *et al.* (2007) Detection of individual gas molecules adsorbed on graphene. *Nat. Mater.*, **6** (9), 652–655.
2. Lee, C. *et al.* (2008) Measurement of the elastic properties and intrinsic strength of monolayer graphene. *Science*, **321** (5887), 385–388.
3. Xiao, N. *et al.* (2011) Enhanced thermopower of graphene films with oxygen plasma treatment. *ACS Nano*, **5** (4), 2749–2755.
4. Eda, G., Fanchini, G., and Chhowalla, M. (2008) Large-area ultrathin films of reduced graphene oxide as a transparent and flexible electronic material. *Nat. Nanotechnol.*, **3** (5), 270–274.
5. Wu, Q. *et al.* (2010) Supercapacitors based on flexible graphene/polyaniline nanofiber composite films. *ACS Nano*, **4** (4), 1963–1970.
6. Novoselov, K.S. *et al.* (2004) Electric field in atomically thin carbon films. *Science*, **306** (5696), 666–669.
7. Obraztsov, A.N. *et al.* (2007) Chemical vapor deposition of thin graphite films of nanometer thickness. *Carbon*, **45** (10), 2017–2021.
8. Gattia, D.M., Vittori Antisari, M., and Marazzi, R. (2007) AC arc discharge synthesis of single-walled nanohorns and highly convoluted graphene sheets. *Nanotechnology*, **18** (25), 255604.
9. Hummers, W.S. Jr., and Offeman, R.E. (1958) Preparation of graphitic oxide. *J. Am. Chem. Soc.*, **80** (6), 1339.
10. Van Bommel, A.J., Crombeen, J.E., and Van Tooren, A. (1975) LEED and Auger electron observations of the SiC(0001) surface. *Surf. Sci.*, **48** (2), 463–472.
11. Wang, Z. *et al.* (2009) Direct electrochemical reduction of single-layer graphene oxide and subsequent functionalization with glucose oxidase. *J. Phys. Chem. C*, **113** (32), 14071–14075.
12. Choi, K. *et al.* (2013) Terahertz and optical study of monolayer graphene processed by plasma oxidation. *Appl. Phys. Lett.*, **102** (13), 131901.
13. Rani, J.R. *et al.* (2013) Controlling the luminescence emission from palladium grafted graphene oxide thin films via reduction. *Nanoscale*, **5** (12), 5620–5627.
14. Lim, J. *et al.* (2013) Terahertz, optical, and Raman signatures of monolayer graphene behavior in thermally reduced graphene oxide films. *J. Appl. Phys.*, **113** (18).
15. Nair, R.R. *et al.* (2008) Fine structure constant defines visual transparency of graphene. *Science*, **320** (5881), 1308.
16. Meyer, J.C. *et al.* (2007) The structure of suspended graphene sheets. *Nature*, **446** (7131), 60–63.
17. Tung, V.C. *et al.* (2009) High-throughput solution processing of large-scale graphene. *Nat. Nanotechnol.*, **4** (1), 25–29.
18. Ferrari, A.C. *et al.* (2006) Raman spectrum of graphene and graphene layers. *Phys. Rev. Lett.*, **97** (18), 187401.
19. Rani, J.R. *et al.* (2013) Substrate and buffer layer effect on the structural and optical properties of graphene oxide thin films. *RSC Adv.*, **3** (17), 5926–5936.
20. Bao, Q. *et al.* (2010) Graphene-polymer nanofiber membrane for ultrafast photonics. *Adv. Funct. Mater.*, **20** (5), 782–791.
21. Gokus, T. *et al.* (2009) Making graphene luminescent by oxygen plasma treatment. *ACS Nano*, **3** (12), 3963–3968.
22. Bostwick, A. *et al.* (2008) Photoemission studies of graphene on SiC: growth, interface, and electronic structure. *Adv. Solid State Phys.*, **47**, 159–170.
23. Virojanadara, C. *et al.* (2008) Homogeneous large-area graphene layer growth on 6H-SiC(0001). *Phys. Rev. B: Condens. Matter*, **78** (24), 245403.
24. Sutter, P.W., Flege, J.I., and Sutter, E.A. (2008) Epitaxial graphene on ruthenium. *Nat. Mater.*, **7** (5), 406–411.
25. N'Diaye, A.T. *et al.* (2008) Structure of epitaxial graphene on Ir(111). *New J. Phys.*, **10**.
26. Otero, G. *et al.* (2010) Ordered vacancy network induced by the growth of epitaxial graphene on Pt(111). *Phys. Rev. Lett.*, **105** (21), 216102.
27. Regan, W. *et al.* (2010) A direct transfer of layer-area graphene. *Appl. Phys. Lett.*, **96** (11), 113102.
28. Green, A.A. and Hersam, M.C. (2009) Solution phase production of graphene

with controlled thickness via density differentiation. *Nano Lett.*, **9** (12), 4031–4036.
29. Ziambaras, E. *et al.* (2007) Potassium intercalation in graphite: a van der Waals density-functional study. *Phys. Rev. B: Condens. Matter*, **76** (15), 155425.
30. McAllister, M.J. *et al.* (2007) Single sheet functionalized graphene by oxidation and thermal expansion of graphite. *Chem. Mater.*, **19** (18), 4396–4404.
31. Stankovich, S. *et al.* (2007) Synthesis of graphene-based nanosheets via chemical reduction of exfoliated graphite oxide. *Carbon*, **45** (7), 1558–1565.
32. Compton, O.C. *et al.* (2010) Electrically conductive "alkylated" graphene paper via chemical reduction of amine-functionalized graphene oxide paper. *Adv. Mater.*, **22** (8), 892–896.
33. Chandra, V. *et al.* (2010) Water-dispersible magnetite-reduced graphene oxide composites for arsenic removal. *ACS Nano*, **4** (7), 3979–3986.
34. Zhu, X. *et al.* (2011) Reduced graphene oxide/tin oxide composite as an enhanced anode material for lithium ion batteries prepared by homogenous coprecipitation. *J. Power Sources*, **196** (15), 6473–6477.
35. Wu, Z.S. *et al.* (2012) Graphene/metal oxide composite electrode materials for energy storage. *Nano Energy*, **1** (1), 107–131.
36. Feng, H., Li, Y., and Li, J. (2012) Strong reduced graphene oxide-polymer composites: hydrogels and wires. *RSC Adv.*, **2** (17), 6988–6993.
37. Bai, H. *et al.* (2011) Graphene oxide/conducting polymer composite hydrogels. *J. Mater. Chem.*, **21** (46), 18653–18658.
38. Li, B. *et al.* (2011) Cu 2O@reduced graphene oxide composite for removal of contaminants from water and supercapacitors. *J. Mater. Chem.*, **21** (29), 10645–10648.
39. Stankovich, S. *et al.* (2006) Graphene-based composite materials. *Nature*, **442** (7100), 282–286.
40. Zhou, X. *et al.* (2009) In situ synthesis of metal nanoparticles on single-layer graphene oxide and reduced graphene oxide surfaces. *J. Phys. Chem. C*, **113** (25), 10842–10846.
41. Shen, J. *et al.* (2011) One-pot hydrothermal synthesis of Ag-reduced graphene oxide composite with ionic liquid. *J. Mater. Chem.*, **21** (21), 7795–7801.
42. Chen, G.H. *et al.* (2001) Dispersion of graphite nanosheets in a polymer matrix and the conducting property of the nanocomposites. *Polym. Eng. Sci.*, **41** (12), 2148–2154.
43. Binnig, G., Quate, C.F., and Gerber, C. (1986) Atomic force microscope. *Phys. Rev. Lett.*, **56** (9), 930–933.
44. Lang, K.M. *et al.* (2004) Conducting atomic force microscopy for nanoscale tunnel barrier characterization. *Rev. Sci. Instrum.*, **75** (8), 2726–2731.
45. Gross, L. *et al.* (2009) The chemical structure of a molecule resolved by atomic force microscopy. *Science*, **325** (5944), 1110–1114.
46. Parades, J.I. *et al.* (2008) Graphene oxide dispersions in organic solvents. *Langmuir*, **24** (19), 10560–10564.
47. Paredes, J.I. *et al.* (2009) Atomic force and scanning tunneling microscopy imaging of graphene nanosheets derived from graphite oxide. *Langmuir*, **25** (10), 5957–5968.
48. Singh, V. *et al.* (2011) Graphene based materials: past, present and future. *Prog. Mater. Sci.*, **56** (8), 1178–1271.
49. Kim, K.S. *et al.* (2009) Large-scale pattern growth of graphene films for stretchable transparent electrodes. *Nature*, **457** (7230), 706–710.
50. Barlow, W. (1883) Probable nature of the internal symmetry of crystals. *Nature*, **29** (738), 186–188.
51. Sohncke, L. (1884) Probable nature of the internal symmetry of crystals. *Nature*, **29** (747), 383–384.
52. Compton, A.H. (1923) A quantum theory of the scattering of X-rays by light elements. *Phys. Rev.*, **21** (5), 483–502.
53. Bragg, W.H. (1908) The nature of γ and X-rays. *Nature*, **77** (1995), 270–271.
54. Bragg, W.H. (1910) XXXIX. The consequence of the corpuscular hypothesis of the γ and X rays, and the range of β rays. *Philos. Mag. Ser. 6*, **20** (117), 385–416.

55. Bragg, W. (1912) On the direct or indirect nature of the ionization by X-rays. *Philos. Mag.*, **23**, 647–650.
56. von Laue, M. (1915) Concerning the Detection of X-ray Interferences. Nobel Lecture, *http//www.nobelprize.org/nobel_prizes/physics/laureates/1914/* (accessed 30 August 2014).
57. Ford, W.E. and Dana, E.S. (1932) *A Textbook of Mineralogy*, John Wiley & Sons, Inc., New York, p. 438.
58. Bragg, W. (1913) The structure of some crystals as indicated by their diffraction of X-rays. *Proc. R. Soc. London, Ser. A*, **89** (610), 248–277.
59. Bragg, W., James, R.t., and Bosanquet, C. (1921) The intensity of reflexion of X-rays by rock-salt.—Part II. *London, Edinburgh Dublin Philos. Mag. J. Sci.*, **42** (247), 1–17.
60. Bragg, W.L. (1914) The analysis of crystals by the X-ray spectrometer. *Proc. R. Soc. London, Ser. A*, **89** (613), 468–489.
61. Culity, B. and Stock, S. (1978) *Elements of X-ray Diffraction*, Edison Wesley, London.
62. Hye-Mi, Ju, Seung Hun, Huh, Seong-Ho, Choi, Hong-Lim, Lee (2010) Structures of thermally and chemically reduced graphene, Materials Letters, **64**, (3), 357–360, ISSN 0167-577X, *http://dx.doi.org/10.1016/j.matlet.2009.11.016.* (*http://www.sciencedirect.com/science/article/pii/S0167577X0900857X*)
63. Li, Z. *et al.* (2007) X-ray diffraction patterns of graphite and turbostratic carbon. *Carbon*, **45** (8), 1686–1695.
64. Huh, S.H. (2011) *Thermal Reduction of Graphene Oxide*, Chapter, INTECH.
65. Lim, J. *et al.* (2013) Terahertz, optical, and Raman signatures of monolayer graphene behavior in thermally reduced graphene oxide films. *J. Appl. Phys.*, **113** (18), 183502–183502-5.
66. Rani, J. *et al.* (2012) Epoxy to carbonyl group conversion in graphene oxide thin films: effect on structural and luminescent characteristics. *J. Phys. Chem. C*, **116** (35), 19010–19017.
67. Zhou, S. *et al.* (2007) Substrate-induced bandgap opening in epitaxial graphene. *Nat. Mater.*, **6** (10), 770–775.
68. Saxena, S., Tyson, T.A., and Negusse, E. (2010) Investigation of the local structure of graphene oxide. *J. Phys. Chem. Lett.*, **1** (24), 3433–3437.
69. Titelman, G. *et al.* (2005) Characteristics and microstructure of aqueous colloidal dispersions of graphite oxide. *Carbon*, **43** (3), 641–649.
70. Wallace, P. (1947) The band theory of graphite. *Phys. Rev.*, **71** (9), 622.
71. Geim, A.K. and Novoselov, K.S. (2007) The rise of graphene. *Nat. Mater.*, **6** (3), 183–191.
72. Charlier, J.-C. *et al.* (2008) *Electron and Phonon Properties of Graphene: their Relationship with Carbon Nanotubes, in Carbon Nanotubes*, Springer, pp. 673–709.
73. Lemme, M.C. *et al.* (2007) A graphene field-effect device. *IEEE Electron Device Lett.*, **28** (4), 282–284.
74. Casiraghi, C. *et al.* (2007) Rayleigh imaging of graphene and graphene layers. *Nano Lett.*, **7** (9), 2711–2717.
75. Blake, P. *et al.* (2007) Making graphene visible. *Appl. Phys. Lett.*, **91**, 063124.
76. Hasan, T. *et al.* (2009) Nanotube–polymer composites for ultrafast photonics. *Adv. Mater.*, **21** (38-39), 3874–3899.
77. Lui, C.H. *et al.* (2010) Light emission from graphene induced by femtosecond laser pulses. *Bull. Am. Phys. Soc.*, **1**, Z22.008.
78. Eda, G. *et al.* (2010) Blue photoluminescence from chemically derived graphene oxide. *Adv. Mater.*, **22** (4), 505–509.
79. Hamberg, I. and Granqvist, C.G. (1986) Evaporated Sn-doped In 2 O 3 films: Basic optical properties and applications to energy-efficient windows. *J. Appl. Phys.*, **60** (11), R123–R160.
80. Minami, T. (2005) Transparent conducting oxide semiconductors for transparent electrodes. *Semicond. Sci. Technol.*, **20** (4), S35.
81. Holland, L. and Siddall, G. (1953) The properties of some reactively sputtered metal oxide films. *Vacuum*, **3** (4), 375–391.
82. Granqvist, C.G. (2007) Transparent conductors as solar energy materials: a panoramic review. *Sol. Energy Mater. Sol. Cells*, **91** (17), 1529–1598.

83. Lee, J.-Y. *et al.* (2008) Solution-processed metal nanowire mesh transparent electrodes. *Nano Lett.*, **8** (2), 689–692.

84. De, S. *et al.* (2009) Silver nanowire networks as flexible, transparent, conducting films: extremely high DC to optical conductivity ratios. *ACS Nano*, **3** (7), 1767–1774.

85. Chapin, D., Fuller, C., and Pearson, G. (1954) A new silicon p-n junction photocell for converting solar radiation into electrical power. *J. Appl. Phys.*, **25** (5), 676–677.

86. Green, M.A. *et al.* (1999) Solar cell efficiency tables (version 13). *Prog. Photovoltaics Res. Appl.*, **7** (1), 31–37.

87. Krebs, F.C. (2009) All solution roll-to-roll processed polymer solar cells free from indium-tin-oxide and vacuum coating steps. *Org. Electron.*, **10** (5), 761–768.

88. Burroughes, J. *et al.* (1990) Light-emitting diodes based on conjugated polymers. *Nature*, **347** (6293), 539–541.

89. Giovannetti, G. *et al.* (2008) Doping graphene with metal contacts. *Phys. Rev. Lett.*, **101** (2), 026803.

90. Saleh, B. and Teich, M. (2007) *Fundamentals of Photonics*, Chapter 7, John Wiley & Sons, Inc., NewYork.

91. Dawlaty, J.M. *et al.* (2008) Measurement of ultrafast carrier dynamics in epitaxial graphene. *Appl. Phys. Lett.*, **92**, 042116.

92. Wright, A., Cao, J., and Zhang, C. (2009) Enhanced optical conductivity of bilayer graphene nanoribbons in the terahertz regime. *Phys. Rev. Lett.*, **103** (20), 207401.

93. Boyd, R.W. (2003) *Nonlinear Optics*, Academic Press.

94. Keller, U. (2003) Recent developments in compact ultrafast lasers. *Nature*, **424** (6950), 831–838.

95. Wang, F. *et al.* (2008) Wideband-tuneable, nanotube mode-locked, fibre laser. *Nat. Nanotechnol.*, **3** (12), 738–742.